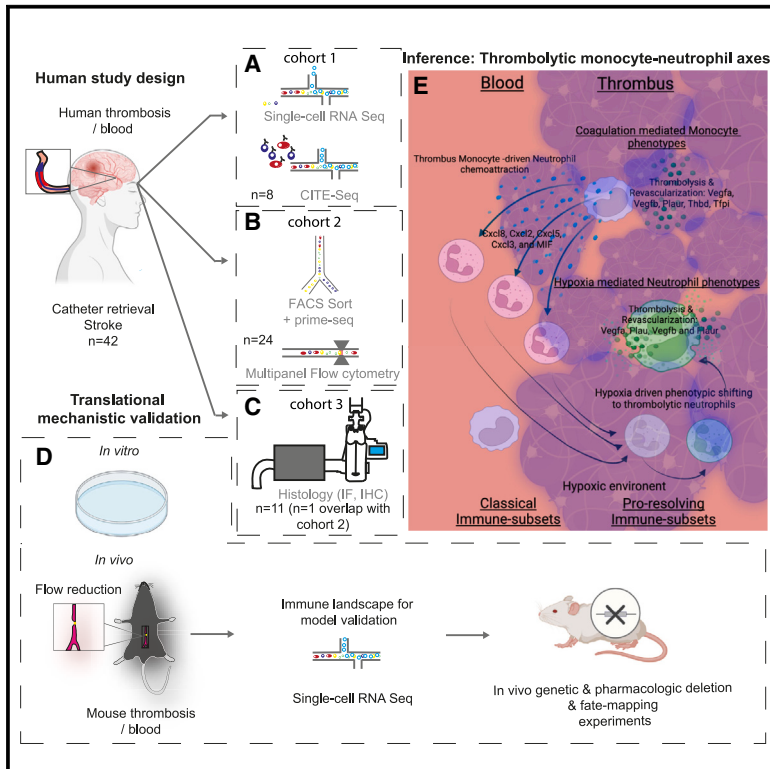


Immunity

Immunothrombolytic monocyte-neutrophil axes dominate the single-cell landscape of human thrombosis and correlate with thrombus resolution

Graphical abstract



Authors

Kami Pekayvaz, Badr Kilani, Markus Joppich, ..., Steffen Massberg, Leo Nicolai, Konstantin Stark

Correspondence

kami.pekayvaz@med.uni-muenchen.de (K.P.),
leo.nicolai@med.uni-muenchen.de (L.N.),
konstantin.stark@med.uni-muenchen.de (K.S.)

In brief

The immune landscape of human and murine thrombosis remains unclear. Pekayvaz et al. map the immune landscape of thrombosis and describe prominent thrombolytic functions of immune cells, a pattern that they term *immunothrombolysis*: neutrophils recruited toward thrombi, attracted by non-classical monocytes, acquire a HIF1 α -mediated thrombus-resolving profile.

Highlights

- This study maps the single-cell landscape of thrombosis and adds mechanistic validation
- This benchmarks novel, specialized immune phenotypes in vascular disease resolution
- Neutrophils are recruited to thrombi by monocytes and acquire a thrombolytic phenotype
- A therapeutically exploitable phenomenon, which we term *immunothrombolysis*



Resource

Immunothrombolytic monocyte-neutrophil axes dominate the single-cell landscape of human thrombosis and correlate with thrombus resolution

Kami Pekayvaz,^{1,2,15,*} Badr Kilani,¹ Markus Joppich,³ Luke Eivers,¹ Sophia Brambs,¹ Viktoria Knottenberg,¹ Sezer Akgöl,¹ Keyang Yue,¹ Lukas Li,¹ Alejandro Martinez-Navarro,¹ Rainer Kaiser,^{1,2} Nina Meißner,⁴ Heiko Schulz,⁵ Larissa Belz,¹ Anastassia Akhalkatsi,¹ Sven Stockhausen,¹ Tonina T. Mueller,^{1,2,7} Simon Millonig,¹ Lea Hartelt,¹ Christoph Gold,^{1,2} Aleksandar Janjic,⁶ Vivien Polewka,¹ Franziska Wendler,¹ Augustin Droste zu Senden,¹ Anna Titova,¹ Alexander Leunig,^{1,2} Michael Voelkl,^{7,8} Bernd Engemann,⁷ Moritz R. Hernandez Petzsche,⁹ Tobias Boeckh-Behrens,⁹ Thomas Liebig,¹⁰ Sandra Winning,¹¹ Joachim Fandrey,¹¹ Martin Dichgans,^{2,4,12,13} Wolfgang Enard,⁶ Ralf Zimmer,³ Steffen Tiedt,⁴ Steffen Massberg,^{1,2} Leo Nicolai,^{1,2,14,*} and Konstantin Stark^{1,2,14,*}

¹Department of Medicine I, University Hospital, LMU Munich, Munich, Germany

²DZHK (German Centre for Cardiovascular Research), partner site Munich Heart Alliance, Munich, Germany

³LFE Bioinformatik, Department of Informatics, Ludwig-Maximilians-Universität München, Munich, Germany

⁴Institute for Stroke and Dementia Research, University Hospital, LMU Munich, Munich, Germany

⁵Institute of Pathology, Ludwig-Maximilians-Universität München, Munich, Germany

⁶Anthropology and Human Genomics, Faculty of Biology, Ludwig-Maximilians-Universität München, Munich, Germany

⁷Institute of Laboratory Medicine, University Hospital, LMU Munich, Munich, Germany

⁸Department of Medicine III, University Hospital, LMU Munich, Munich, Germany

⁹Department of Diagnostic and Interventional Neuroradiology, School of Medicine and Health, Klinikum rechts der Isar, Technical University of Munich, Munich, Germany

¹⁰Institute for Diagnostic and Interventional Neuroradiology, University Hospital, LMU Munich, Munich, Germany

¹¹University of Duisburg-Essen, Institute for Physiology, Essen, Germany

¹²Munich Cluster for Systems Neurology (SyNergy), Munich, Germany

¹³German Center for Neurodegenerative Diseases (DZNE, Munich), Munich, Germany

¹⁴These authors contributed equally

¹⁵Lead contact

*Correspondence: kami.pekayvaz@med.uni-muenchen.de (K.P.), leo.nicolai@med.uni-muenchen.de (L.N.), konstantin.stark@med.uni-muenchen.de (K.S.)

<https://doi.org/10.1016/j.immuni.2025.03.020>

SUMMARY

Thrombotic diseases remain the major cause of death and disability worldwide, and the contribution of inflammation is increasingly recognized. Thromboinflammation has been identified as a key pathomechanism, but an unsupervised map of immune-cell states, trajectories, and intercommunication at a single-cell level has been lacking.

Here, we reveal innate leukocyte substates with prominent thrombolytic properties by employing single-cell omics measures on human stroke thrombi. Using *in vivo* and *in vitro* thrombosis models, we propose a pro-resolving monocyte-neutrophil axis, combining two properties: (1) NR4A1^{hi} non-classical monocytes acquire a thrombolytic and neutrophil-chemoattractive phenotype, and (2) blood neutrophils are thereby continuously recruited to established thrombi through CXCL8-CXCR1 and CXCR2 and adopt a hypoxia-induced thrombus-resolving urokinase receptor (PLAUR)⁺ phenotype. This immunothrombolytic axis results in thrombus resolution. Together, with this immune landscape of thrombosis, we provide a valuable resource and introduce the concept of “immunothrombolysis” with broad mechanistic and translational implications at the crossroad of inflammation and thrombosis.

INTRODUCTION

Thrombosis and thromboembolism are a major global cause of morbidity and mortality by leading to myocardial infarction, stroke, and venous thromboembolism.^{1,2} Simultaneously, anti-

thrombotic therapies carry a relevant risk of bleeding complications and are only partially effective in preventing thrombotic events.^{1,2} A strong interdependence between inflammation and thrombosis has gathered increasing attention in recent years, a process termed “immunothrombosis” (in physiological



processes) or “thromboinflammation” (in disease scenarios).¹ Studies involving rodent thrombosis models identified multiple therapeutically targetable inflammatory mechanisms in both low- and high-shear clot formation that set off a thrombotic *vicious cycle* between neutrophils, monocytes, platelets, and the coagulation system.^{3–9} In humans, histological analyses confirm a high frequency of leukocytes, particularly neutrophils, in cerebral and coronary thrombi.^{10–13} While highly valuable for initiating the translation of the concept of thromboinflammation to humans, these studies are limited to descriptive morphological and numerical conclusions. To date, unsupervised maps of trajectories, functional states, and intercommunication, particularly of leukocytes in human thrombosis, are yet to be defined. Most mechanistic studies involving neutrophils and monocytes in thromboinflammation focused on the initiation of thrombosis but not on established thrombi. Hence, whether innate immune cells further aggravate established thrombosis or might even adopt protective roles remains unclear. Along these lines, the function of neutrophils in thrombosis remains complex and context dependent: in the initiation of thrombosis, neutrophils have been identified to promote clot formation,⁴ yet certain studies also suggest protective roles of innate immune cells in thrombosis, myocardial infarction, and atherosclerosis.^{14–16} Recently, the neutrophil compartment has gathered attention for its transcriptomic plasticity within the circulation and across tissues, allowing environment-imprinted adoption of unexpected phenotypic programs, enabling functional heterogeneity of neutrophils.^{17–21} Similarly, distinct non-classical monocyte subsets have been shown to adopt relevant roles in continuously sustaining vascular homeostasis.²²

We therefore hypothesized that myeloid leukocyte subsets might adopt distinct, non-canonical phenotypes in local thrombi to perform specialized tasks that in turn allow modulation of the thrombotic microenvironment. To allow a first unsupervised characterization of the immune landscape in established thrombosis, we performed a state-of-the-art multi-omic characterization of human thrombi and mapped the trajectories, functional states, and intercommunication of immune cells and platelet-leukocyte aggregates in thrombosis at single-cell resolution. Particularly, we found a prominent thrombolytic and angiogenic neutrophil population, induced by hypoxia-mediated signaling. We suggest a continuous recruitment of neutrophils, feeding the thrombus neutrophil (tNeutro) population, by local pro-resolving non-classical monocytes.

In summary, this work uncovers the immune-cell landscape of thrombosis by single-cell RNA sequencing (scRNA-seq) and depicts (1) continuously infiltrating tNeutro substates that acquire thrombolytic properties fueled by non-classical-like, pro-resolving thrombus monocytes (tMonos) and a hypoxic microenvironment, thereby (2) establishing the concept of “immunothrombolysis,” and—simultaneously—(3) providing a broadly available resource of the human and murine immune landscape in thrombosis for future research.

RESULTS

Study design

To uncover the inflammatory signature of human thrombosis, we analyzed thrombi and peripheral blood from stroke pa-

tients (Table S1). This allowed standardized large-scale access to human thrombosis (from $n = 32$ subjects for multi-omic analyses) with rapid and standardized *ex vivo* processing protocols, particularly important for neutrophil assessment (see STAR Methods). We performed multi-color flow cytometry to assess overall frequencies of immune-cell subsets. scRNA-seq and cellular indexing of transcriptomes and epitopes by sequencing (CITE-seq) were used to study cell phenotypes, developmental trajectories, functional programs, and cross-communication between immune subsets in thrombosis (cohort description specified in Table S1). For validation, we employed stroke thrombi from an independent second cohort, utilizing a bulk RNA-seq approach of fluorescence-activated cell sorting (FACS) sorted immune cells (prime-seq²⁰) from blood and thrombi. In a reverse translational approach, we utilized an *in vivo* mouse thrombosis model and *in vitro* assays to validate the disease sequelae of the monocyte-neutrophil interplay, identified in human thrombi.

Single-cell-based transcriptomics and surface profiling reveal prominent shifts between blood and thrombus with specialized immune subsets

First, to determine the leukocyte subsets involved in thrombosis, we utilized a flow cytometry-based phenotyping approach with subsequent dimensionality reduction by t-SNE and FlowSOM-based unsupervised clustering (Figures 1A–1C; Figure S1A). Paired comparisons of thrombi with blood from the same patients revealed distinct quantitative differences between blood and thrombi (Figures 1A–1G; Figure S1). We found relative enrichment of distinct neutrophil subsets in thrombi, while most other leukocyte populations, including CD3⁺ T cells, CD19⁺ B cells, or CD56⁺ natural killer (NK) cells and myeloid dendritic cells, were less frequent in thrombi compared with blood. CD123⁺ basophils but not eosinophils were depleted in thrombi compared with blood, while plasmacytoid dendritic cell frequencies and monocyte counts stayed constant between blood and thrombi. tNeutros were characterized by two different phenotypes—a distinct sideward scatter (SSC)^{lo} and an SSC^{hi} phenotype (Figures 1D–1G). The most frequent immune-cell subsets that constituted the thrombus microenvironment were neutrophils and monocytes (Figures 1A–1G; Figure S1).

To generate an immune-cell atlas and further delineate these phenotypic differences, we performed scRNA-seq of retrieved thrombi and simultaneously collected peripheral blood leukocytes. UMAP-based dimensionality reduction showed strong shifts in the immune-cell phenotype (Figure 1H). Further elaboration on immune-cell subclusters comparing blood and thrombi confirmed the predominance of innate immune cells, which also underwent the strongest changes in human thrombosis (in high shear as well as in low shear thrombi) (Figures 1H–1J; Figures S2A–S2G; Table S2). Co-expression analysis of platelet-derived genes revealed cluster 6 monocytes and cluster 14 neutrophils to express relevant amounts of integrin alpha 2B (ITGA2B), suggesting platelet-leukocyte aggregates (Figure S2H). CITE-seq for CD41 expression in blood leukocytes, human thrombus leukocytes, and leukocytes from an artificially generated *in vitro* thrombus revealed particularly cluster 3 and cluster 6 monocytes to show relevant proportions

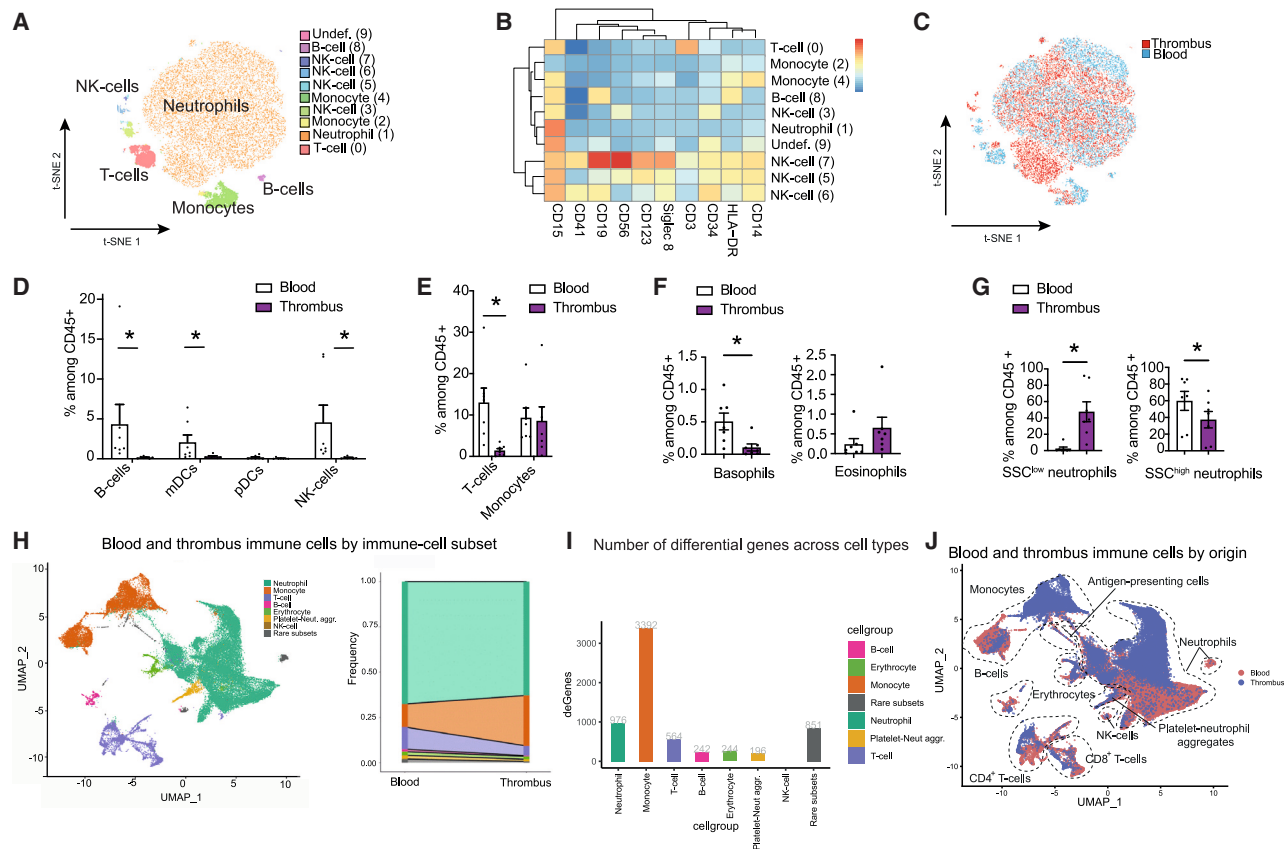


Figure 1. Thrombus immune-cell microenvironment

- (A) Flow cytometry-based immune-cell phenotyping of human thrombosis. t-SNE-based dimensionality reduction, cluster identification with FlowSOM.
- (B) Heatmap of the surface marker expression of each subcluster relative to the maximum expression of the surface marker. See STAR Methods for the exact clustering of the heatmap.
- (C) Color-coded t-SNE, dividing cells by origin from either thrombus or blood.
- (A–C) Depicts one representative thrombus and matched blood (representative of $n = 7$ thrombi and blood).
- (D–G) Quantification of immune cells relative to all CD45⁺ leukocytes in thrombus compared with blood. Flow cytometry phenotyping. $n = 7$ thrombi & blood. Paired t test was used for normally distributed data, and Wilcoxon matched-pairs signed rank test was used for non-parametrically distributed data. $^*p < 0.05$.
- (H) UMAPs of human thrombus and blood scRNA-seq data colored by cell clusters (left), cluster frequencies (with the same color code as the clusters in UMAP) shown for blood or thrombus (right).
- (I) Numbers of differentially regulated genes in-between blood and thrombus immune-cell subsets, allowing quantification of phenotypic shifts between leukocyte subsets in blood and thrombi.
- (J) UMAP of human blood and thrombus scRNA-seq data colored by origin (purple depicts thrombus-derived cells, gray depicts blood-derived cells).
- (H–J) scRNA-seq analyses based on $n = 7$, thrombi; $n = 6$, blood. This figure is also related to Figures S1–S3 and Tables S1 and S2.

of CD41 co-expression, most prominently within *in vivo* and also in artificial *in vitro* thrombosis (see methods for artificial *in vitro* thrombus formation) (Figures S2H–S2L; Table S2). To check whether distinct blood-borne differences (introduced by the thrombectomy intervention) might influence the major effects between blood and thrombi, we checked the robustness of our findings by including a second cohort of blood from healthy subjects in a published in-house dataset.²¹ Comparison of either blood from stroke patients (with respective acute inflammatory responses) or blood from healthy subjects with stroke thrombi showed a high correlation of differentially regulated genes between both types of blood and thrombus, indicating that even major inflammatory blood-borne shifts do not influence the strong shifts observed between blood and thrombi (Figure S2M).

tNeutros possess distinct thromboinflammatory and pro-resolving properties

Neutrophil-specific surface marker profiling recapitulated the presence of both CD15⁺ SSC^{lo} and SSC^{hi} neutrophil subsets. The CD15⁺ SSC^{lo} neutrophil subset was further defined by lower CD16 expression and was enriched in thrombi (Figures S3A and S3B). As short-lived cells, in the setting of thrombosis, CD16^{lo} tNeutros might represent hyperactivated, pre-terminal neutrophil phenotype stages as similarly described previously.^{23–26} Unsupervised, fine-grained subclustering of the tNeuro landscape by scRNA-seq revealed more detailed insights into thrombus and blood neutrophil heterogeneity (Figures 2A–2C). In total, we identified 13 neutrophil subclusters (Figures 2A–2C; Figure S3C). Particularly, the VEGFA^{hi} CD16^{hi} cluster 2 was confined to thrombi. Neutrophil vascular

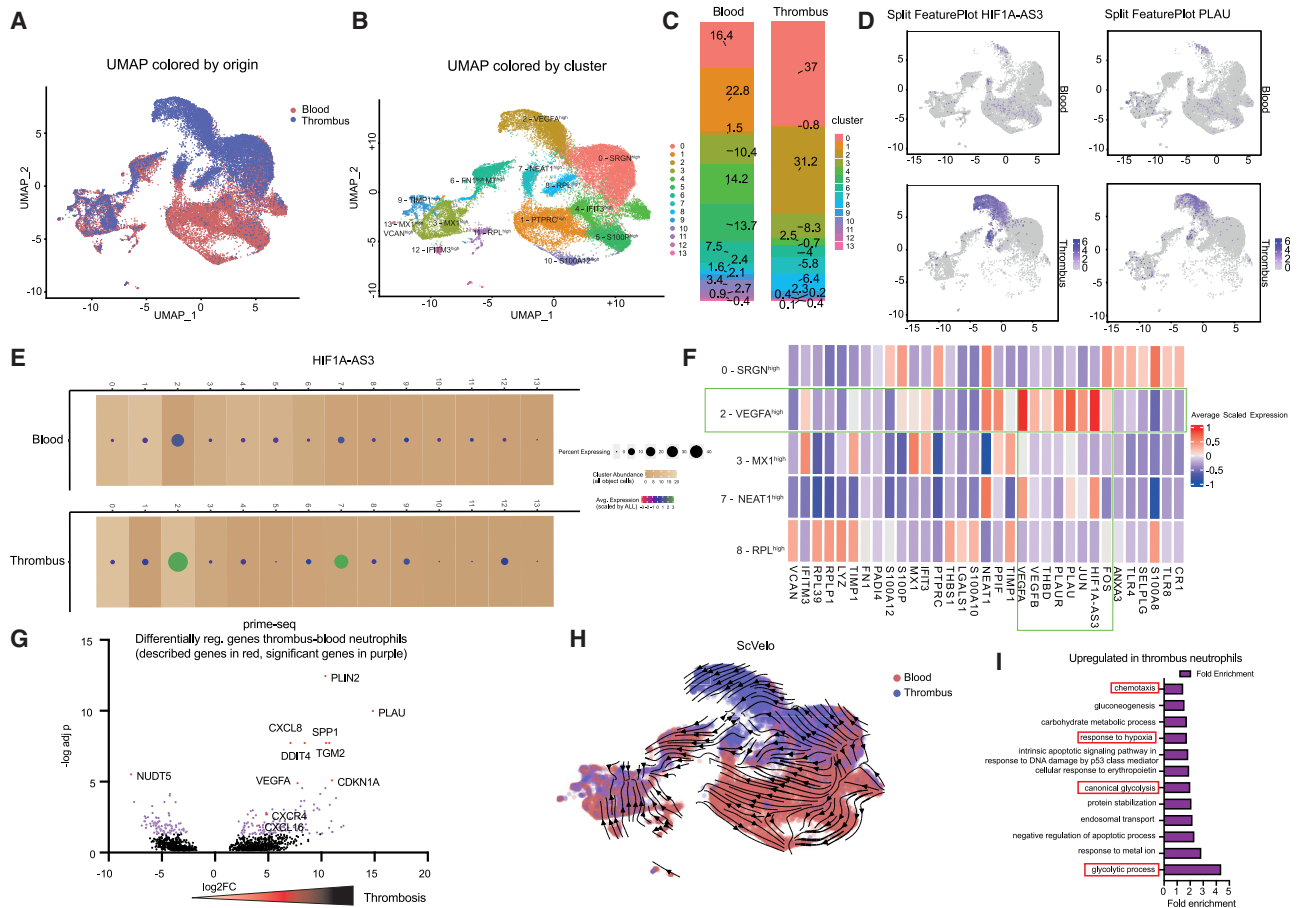


Figure 2. A detailed neutrophil atlas delineates subsets with prominent thrombus-resolving properties

(A) scRNA-seq UMAP of human blood and tNeutros, reclustered from Figure 1H thrombi, colored by origin (purple depicts thrombus-derived neutrophils, gray depicts blood-derived neutrophils).
 (B) scRNA-seq UMAP of human thrombus and blood single neutrophils colored by neutrophil clusters.
 (C) Frequencies of neutrophil clusters from scRNA-seq data in blood and thrombus in %.
 (D) FeaturePlots of *HIF1A-AS3* and *PLAU* expression in blood and tNeutros.
 (E) Enhanced dotplot of *HIF1A-AS3* expression across different clusters in blood or thrombi, including average expression, cell abundance, and percentage of expressing cells of each cluster (legend added to the figure).
 (F) Heatmap depicting selected cluster-defining genes with functional relevance of cells from thrombus clusters or joint blood-thrombus clusters. Cluster 2, the main tNeuro cluster, and its respective functional cluster-defining genes are highlighted by a green box.
 (G) Volcano plot of differentially regulated genes between blood and tNeutros as determined by prime-seq²⁰ of FACS-sorted neutrophils. $n = 8$ thrombi, $n = 9$ blood (independent cohort). Upregulated genes in thrombi are depicted on the right (as shown by the arrow).
 (H) Velocity analysis by scVelo. Arrows depict the calculated velocity vector field displayed as streamlines to determine cellular fate trajectories.
 (I) Gotermin_BP_Direct analysis with genes enriched in tNeutros compared with blood neutrophils. $n = 8$ thrombi, $n = 9$ blood. This figure is also related to Figure S3.

endothelial growth factor A (VEGFA) secretion has been associated with a pro-angiogenic, pro-resolving phenotype.¹⁹ Simultaneously, SRGN^{hi} cluster 0, NEAT1^{hi} cluster 7, and ribosomal protein (RPL)^{hi} cluster 8 were enriched in thrombi, whereas MX1^{hi} cluster 3 and mitochondrial gene (MT)^{hi} cluster 6 showed comparable frequency in blood and thrombi (Figures 2A–2C; Figure S3C). Clusters 0, 2, 3, 7, and 8 accounted for ~90% of profiled tNeutros. To allow an integrative analysis of the surface proteome and transcriptome of neutrophils, we performed CITE-seq²⁷ in a subset of thrombi and blood. This generally confirmed the correlation of neutrophil clusters with low CD16 surface expression on a protein level with low CD16 (FCGR3A) gene expression (Figure S3D). However, the shift to-

ward CD16^{lo} neutrophil subsets as observed in flow cytometry was not prominent in the scRNA-seq approach, possibly due to the known limitations of neutrophil RNA-seq approaches (i.e., low RNA content) and the matured/pre-terminal nature of the CD16^{lo} tNeuro subsets.

Next, we sought to analyze the dominant tNeuro clusters in detail. We found that tNeutros expressed high amounts of hypoxia-associated genes such as *HIF1A-AS3* in addition to genes associated with a thrombus-resolving phenotype such as plasminogen activator urokinase (*PLAU*) (Figures 2D and 2E). The intracellular proteoglycan serglycin (SRGN^{hi} cluster 0) was enriched in inflammatory transcripts like Toll-like receptor 4 and 8 (TLR4 and 8), as well as S100A proteins and receptors

like complement receptor 1 and P-selectin ligand (Figure 2F; Figure S3C). Many of these enriched genes are also implicated in pro-thrombotic neutrophil extracellular trap formation (NETosis).^{28–33} Interferon-induced GTP-binding protein Mx1 (MX1^{hi}) cluster 3 showed upregulation of interferon stimulated genes (ISGs) like MX1, interferon-induced protein with tetratricopeptide repeats 3 (IFIT3), and interferon-induced transmembrane protein 3 (IFITM3), also pointing toward a host defense signature. RPL^{hi} (encoding ribosomal protein-related genes) cluster 8 abundantly expressed ribosomal genes, indicating high translational activity, as well as pro-thrombotic thrombospondin 1 (THBS1) transcription (Figure 2F; Figure S3C).

FN1 (encoding fibronectin), a glycoprotein centrally involved in hemostasis^{34,35} and involved in clot stabilization when incorporated into the fibrin network³⁵ was expressed predominantly by FN1^{hi} cluster 6 (Figure S3E). The transcriptome of cluster 6 was dominated by high FN1 expression. S100P^{hi} cluster 5 and S100A12^{high} cluster 10 also expressed high amounts of protein-arginine deiminase type-4 (PADI4), possibly representing pro-NETotic neutrophils,^{36–41} fueling thrombosis¹ (Figure S3E). This indicates the presence of multiple neutrophil clusters, which upregulate proteins known to drive thromboinflammation and propagate thrombosis.

This contrasted with thrombus-exclusive VEGFA^{hi} and VEGFB^{hi} cluster 2, characterized by high expression of FOS and hypoxia-associated HIF1A-AS3, as well as anti-thrombotic urokinase (PLAU), urokinase receptor (PLAUR), and thrombospondin (THBD) (Figure 2F). Feature plots confirmed high amounts of hypoxia-associated genes such as HIF1A-AS3 in addition to genes associated with a thrombus-resolving phenotype such as PLAU in thrombi (Figures 2D and 2E).

We validated global transcriptomic changes of tNeutros by prime-seq²⁰ of flow cytometry-sorted neutrophils from thrombi and respective blood samples, including prominent upregulation of pro-resolving pathways (PLAU and VEGFA). Indeed, the most strongly enriched gene across tNeutros was PLAU (Figure 2G; Figure S3F). In summary, we define heterogeneous populations of neutrophils in human thrombi, which differ phenotypically from circulating neutrophils. Moreover, our scRNA-seq data provide evidence of tNeuro subsets with diverse, potentially diametrical effector functions: pro-thrombotic and NETotic populations as well as pro-resolving subsets with hypoxic attributes.

Due to these strong shifts culminating in separately clustering immune-cell subsets, we asked whether neutrophils emerge from their phenotypically nearest blood counterparts. A cell trajectory inference by scVelo⁴² suggested anti-thrombotic tNeutros (VEGFA^{hi} cluster 2) as well as other tNeuro subsets to phenotypically shift from common circulating blood neutrophils toward tNeutros. The main vectors from some possible blood progenitors (i.e., cluster 0 SRGN^{high} neutrophils), recovering dynamic information from splicing kinetics on a single-cell level, were directed toward distinct thrombus progeny (cluster 2 VEGFA^{hi} neutrophils) (Figure 2H). This suggests a continuous polarization of blood neutrophils toward tNeutros. However, single-cell-based trajectory analyses do not prove differentiation paths of immune-cell subsets but provide hypotheses that require future fate-mapping approaches for different leukocyte subsets within thrombosis. In summary, tNeutros form a heterogeneous

population with differential pro-thrombotic as well as thrombolytic properties.

Hypoxia imprints a pro-resolving phenotype on continuously infiltrating blood neutrophils

To get more functional insight into global changes in tNeutros, we performed a DAVID set enrichment analysis on the Gene Ontology biological process gene sets (GOTERM_BP_DIRECT). This revealed multiple hypoxia-related pathways to be upregulated across tNeutros (Figure 2I). At single-cell resolution HIF1A-AS3 was mainly confined to anti-thrombotic VEGFA^{hi} cluster 2 (Figure 2E). We therefore hypothesized that the hypoxic environment within the thrombus might potentially trigger the distinct shifts in neutrophils toward a pro-resolving phenotype. The expression of urokinase in tNeutros was indeed confirmed by immunofluorescence (Figure 3A). *In vitro*, we observed that pharmacological HIF1 α stabilization by roxadustat recapitulated the shifts that were observed within thrombi encompassing shifts from a CD16^{hi} toward CD16^{lo} neutrophil subset (Figure 3B). Upon gating on living singlet neutrophils, these CD16^{lo} neutrophils showed normal viability (Figure 3C; Figures S3G and S3H). These cells might be hyperactivated and aged/pre-terminal.^{23–26} To mechanistically investigate the *in vivo* relevance of hypoxia signaling in myeloid leukocytes, we employed a mouse model of flow-reduction-induced thrombosis⁴ mimicking low-flow thrombosis found in human cardioembolic stroke, which was the most common entity in our population (Table S1). Indeed, *in vivo*, *Hif1a* deletion in myeloid cells (by employing *Lyz2-cre; hif1a^{fl/fl}* chimera mice) resulted in an exacerbation of thrombosis and in a drop in PLAUR⁺ neutrophils within the thrombus (Figures 3D and 3E), confirming a thrombo-protective role of HIF1 α signaling in myeloid cells. We next analyzed the effect of HIF1 α signaling on neutrophil function. Roxadustat-mediated hypoxia mimicking resulted in faster resolution of thrombosis *in vitro* (Figure 3F). In comparison, in the setting of mimicked hypoxia, neutrophils at the CD16^{lo} spectrum displayed more fibrin clearance than neutrophils at the CD16^{hi} spectrum (Figure 3G). In summary, HIF1 α expression in neutrophils is linked to a pro-resolving phenotype with increased fibrinolytic properties, the inhibition of which exacerbates thrombosis *in vivo*.

tMonos show a non-classical-like phenotype with thrombus-modulating properties and strong neutrophil-attracting features

Next, we focused on tMonos, as they are the second most common leukocyte population in thrombi. Flow cytometry showed a shift in the tMono compartment driven by increased CD16 surface expression with an intact morphological phenotype (Figures 4A and 4B; Figures S4A and S4B), pointing toward a non-classical phenotype. To gain insight into the global transcriptional landscape across tMono subsets, we performed bulk prime-seq²⁰ on flow cytometry/sorted monocytes from thrombi. We confirmed global upregulation of master transcription factor nuclear receptor subfamily 4 group A member 1 (NR4A1), as well as FCGR3A (encoding Fc gamma receptor IIIa, CD16), jointly highlighting tMono phenotypic shifting along a non-classical trajectory (Figure 4C). In addition, thrombus non-classical-like monocytes were characterized by

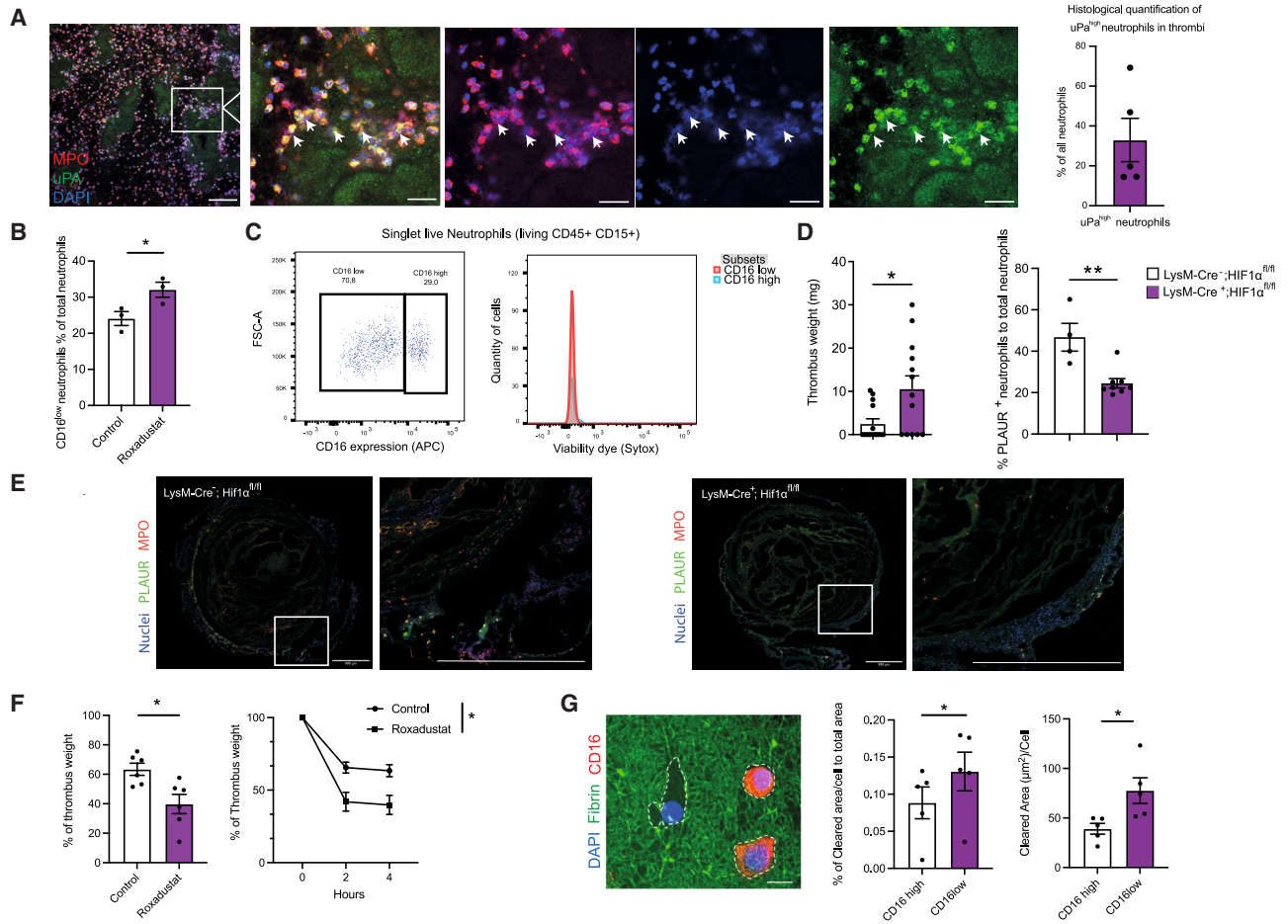


Figure 3. Hypoxia reproduces a CD16^{low} pro-resolving neutrophil phenotype

(A) Left: immunofluorescence imaging of tNeutros (red) stained for urokinase (uPA) (green) and DNA (blue) in cryo-conserved thrombi. Overview: 100 μm , magnified image: 25 μm . Right: histological quantification of uPA^{high} neutrophils in $n = 5$ FPFE thrombi.

(B) Analysis of CD16^{high} and CD16^{low} neutrophil counts (% of living singlets), comparing neutrophils after roxadustat-mediated HIF1 α stabilization with control neutrophils, neutrophils from $n = 3$ independent subjects.

(C) Representative CD16^{high} and CD16^{low} neutrophil gating for SytoxBlue viability dye.

(D) Quantification of thrombus weight in a total of $n = 13$ –14 *Lyz2-cre; HIF1 α ^{fl/fl}* chimera mice (left), histological quantification of PLAUR⁺ neutrophils in thrombi from *Lyz2-cre; HIF1 α ^{fl/fl}* chimera mice (right), $n = 4$ –8 mice.

(E) Representative images (from $n = 4$ –8 mice) of *Lyz2-cre; HIF1 α ^{fl/fl}* chimera thrombi (nuclei in blue with Hoechst staining, MPO in red, and PLAUR in green), scale bar: 500 μm .

(F) Artificial thrombosis weight was quantified in control or roxadustat-treated blood from $n = 6$ individuals 4 h after thrombus induction (left). Longitudinal development of artificial thrombus weight in control or roxadustat-treated blood from $n = 6$ individuals (same data points for the 4 h time point between left and right, illustrated longitudinally) (right), identical experiment with different data depiction.

(G) *In vitro* analysis of fibrin clearance by CD16^{high} or CD16^{low} neutrophils (pretreated with roxadustat) from neutrophils isolated from $n = 5$ different individuals. Scale bar: 10 μm . Paired t test was used for normally distributed paired data, unpaired t test was used for normally distributed unpaired data, Wilcoxon matched-pairs signed rank test was used for non-parametrically distributed data, and Mann-Whitney test was used for non-paired non-parametrically distributed data. * $p < 0.05$. ** $p < 0.01$. This figure is also related to Figure S3.

upregulation of hypoxia or HIF1 α signaling, pro-resolving and fibrinolytic pathways, and most prominently an upregulation of neutrophil chemoattractants and genes associated with host response to pathogens (Figures 4C–4E; Figures S4C–S4E). Next, we dissected the thrombosis-related triggers of monocyte differentiation toward a tMono-like phenotype with thrombolytic and neutrophil-activating properties. Here, we focused on hypoxia and coagulation activation as potential drivers. Even though mimicking hypoxia by roxadustat did not recapitulate the shift in

monocyte phenotype observed within the thrombi (Figure S4F), thrombin-mediated coagulation of whole blood *in vitro* recapitulated a shift of monocytes toward a phenotype with neutrophil-activating properties, indicating that the shift in monocyte phenotype might be directly dependent on the thrombus micro-environment (Figure 4F).

To pinpoint monocyte heterogeneity at single-cell resolution, we performed single-cell RNA-seq and CITE-seq (Figures 5A–5C). Monocytes were clustered in 10 different subsets, with

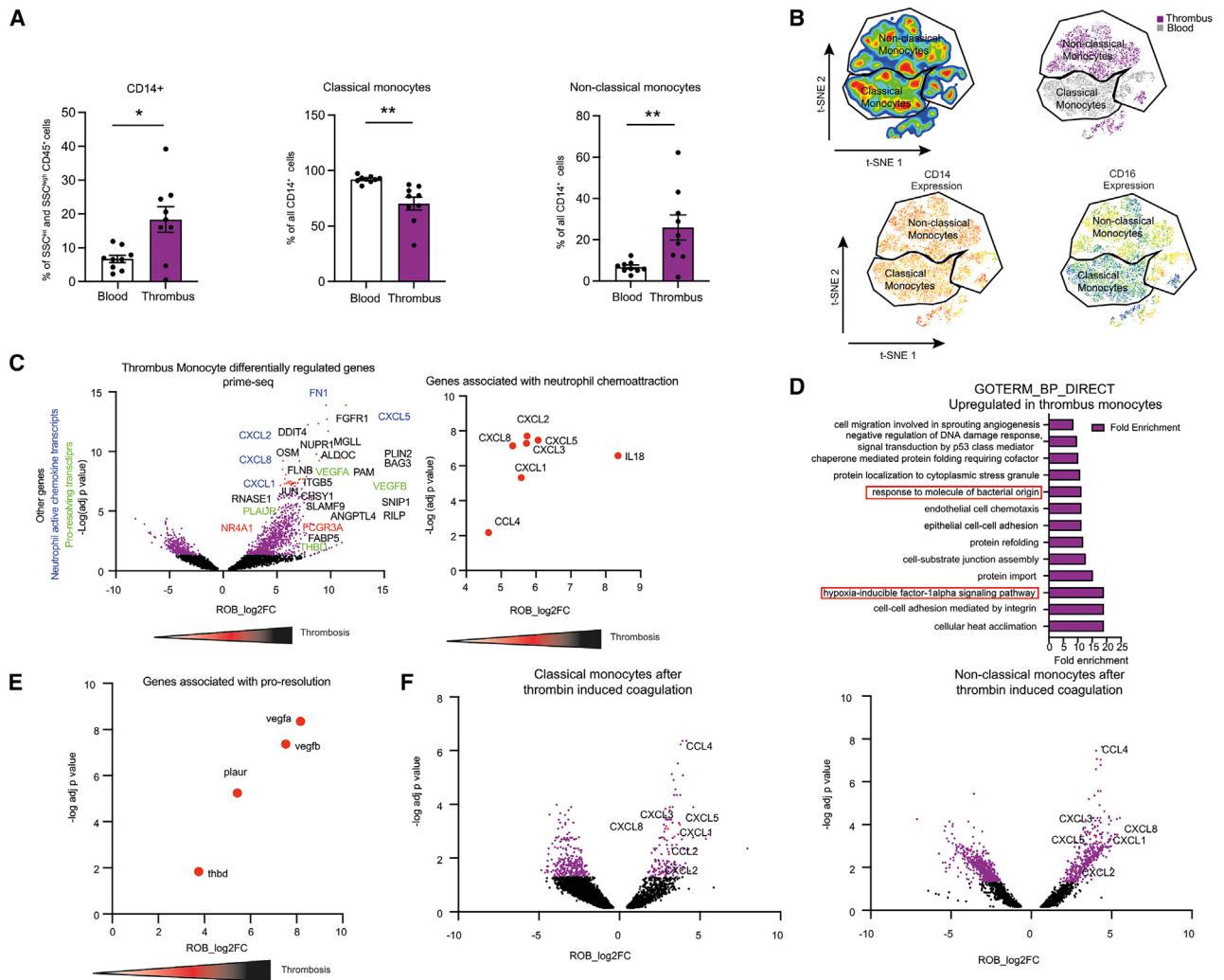


Figure 4. tMonos collectively acquire a non-classical-like, neutrophil-chemoattracting phenotype

(A) Flow cytometry-based quantification of CD14⁺ cells among all CD45⁺ cells present in the classical SSC gates (SSC^{int} or SSC^{high}) and further subdifferentiation classical and non-classical monocytes among all monocytes in blood and thrombi. $n = 9$ blood and $n = 9$ thrombi.

(B) t-SNE based dimensionality reduction of monocyte flow cytometry data further color coded by origin (top right), CD14 expression (bottom left), and CD16 expression (bottom right). Paired t test was used for normally distributed data. $**p < 0.01$.

(C) Volcano plot of differentially regulated genes between blood and tMonos as determined by prime-seq²⁰ of FACS-sorted monocytes (left). Illustration of neutrophil-active chemokines enriched in tMonos as determined by prime-seq²⁰ of FACS-sorted monocytes (right). Upregulated genes in thrombi are depicted on the right side of the axis (as shown by the arrow).

(D) Goterm_BP_Direct analysis with genes enriched in tMonos compared with blood monocytes. The red box depicts the hypoxia-inducible factor-1alpha signaling pathway and response to the molecule of bacterial origin.

(E) Volcano plot of prime-seq²⁰ data of FACS-sorted monocytes specifically depicting upregulated genes associated with recanalization/thrombolysis.

(C–E) $n = 7$ thrombi, $n = 7$ blood.

(F) Volcano plots of differentially regulated genes as determined by prime-seq²⁰ of FACS-sorted classical and non-classical monocytes after thrombin and calcium-mediated induction of the coagulation cascade. Upregulated genes in monocytes isolated after thrombin-induced coagulation are depicted on the right side of the axis (compared with control monocytes). $n = 5$ /group. This figure is also related to Figure S4.

clusters 0 (CLEC5A^{hi}, encoding C-type lectin domain family 5 member A), 3 (THBS1^{high}, encoding thrombospondin 1), 4 (CXCR4^{high}, encoding CXC-motif-chemokine receptor 4), 6 (CXCL8^{hi}, encoding C-X-C motif chemokine ligand 8), 7 (CSTD^{hi}), and 10 representing the most frequent tMono clusters (Figures 5A–5C; Figure S4G). ScVelo⁴²-based differentiation vectors suggested a possible phenotypic shifting of tMonos from respective blood progenitors. CD16 (FCGR3A)^{hi} cluster 9

emerged as the connecting link population between blood and tMonos as evidenced by the developmental trajectories (Figure 5D). Monocle 3¹⁷ also showed that tMono subsets displayed overall higher pseudo-time values than blood monocytes, again associating cluster 9 as one possible linking cluster between blood and tMonos (Figure 5E). This trajectory was based on the expression and distribution of spliced versus unspliced variants of human genes such as ERI1 (encoding

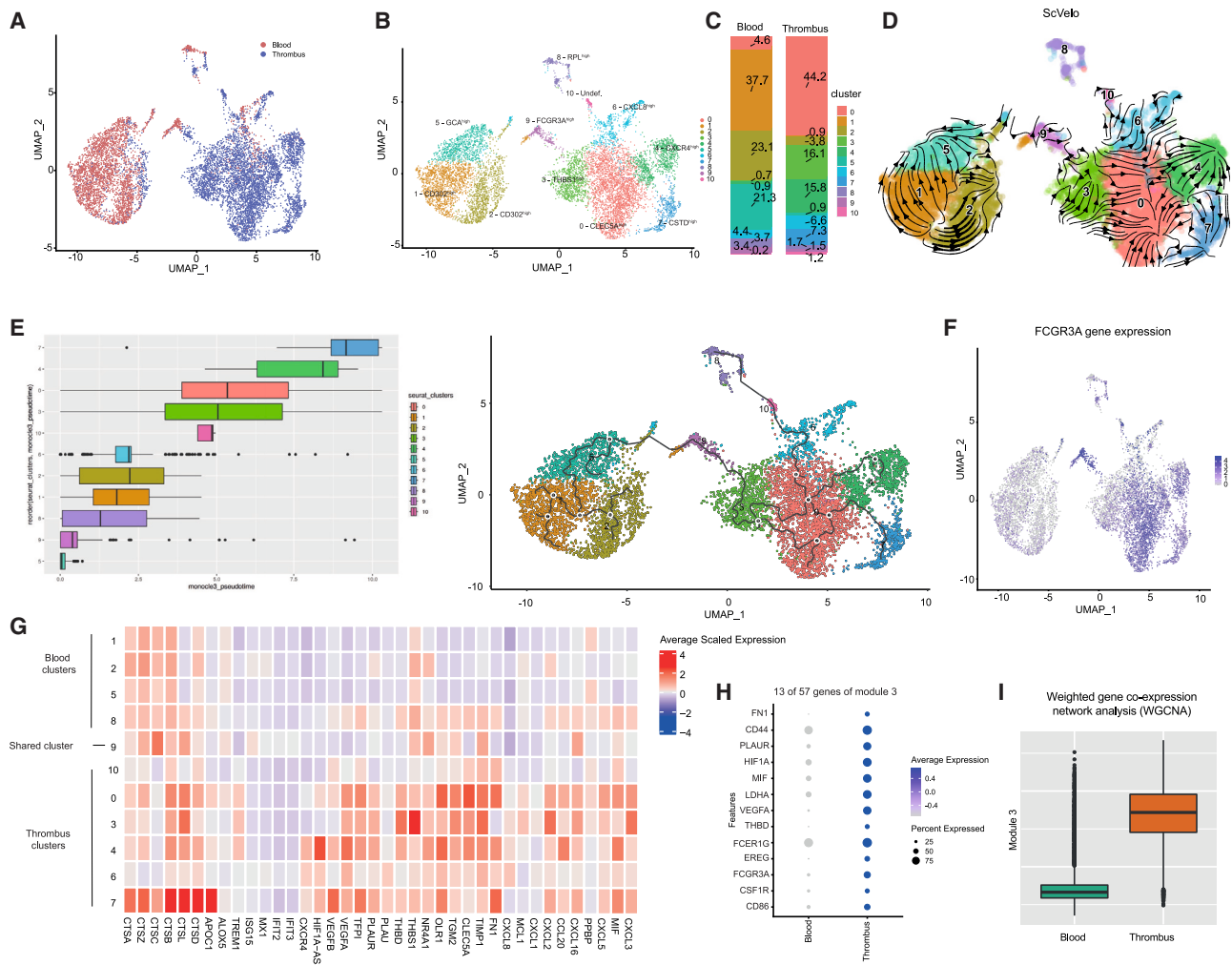


Figure 5. Single-cell resolution delineates multiple functional monocyte clusters with pro-thrombotic, thrombolytic, and neutrophil-attracting tasks that are present in human thrombi

(A) scRNA-seq UMAP of human blood and tMonos, reclustered from Figure 1K, colored by origin (purple depicts thrombus-derived neutrophils, gray depicts blood-derived neutrophils).

(B) scRNA-seq UMAP of human thrombus and blood single monocytes with colored and annotated monocyte clusters.

(C) Frequencies of monocyte clusters in blood and thrombus in % in the scRNA-seq data.

(D) Velocity analysis by scVelo. Arrows are depicting the calculated velocity vector field displayed as streamlines to determine cellular fate trajectories.

(E) Cluster-wise distribution of predicted pseudo-time (left) and pseudo-time trajectories (right) by monocle3.

(F) FeaturePlots of *FCGR3A* (CD16) expression in blood and tNeutros.

(G) Heatmap depicting selected cluster-defining genes with functional relevance of cells from thrombus, blood, and joint blood- tMono clusters from the scRNA-seq data.

(H) Weighted gene co-expression network analysis (WGCNA) of monocytes from the scRNA-seq data, allowing identification of gene networks regulated in a joint manner across cells and tissues. Exemplary inclusion of 14 of a total of 57 genes within identified module 3. Complete module is depicted in Figure S9.

(I) Module score of gene module 3 depicted across blood and thrombus, illustrated as box plots showing median and interquartile range in blood and tMonos from the scRNA-seq data. This figure is also related to Figures S4 and S5.

exoribonuclease 1), substantiating a shift of blood monocytes toward the shared thrombus/blood cluster 9 monocytes (Figure 5D; Figure S4H). Differential analysis revealed *FCGR3A* (encoding CD16) to be strongly enriched beyond cluster 9 across major tMono clusters (Figure 5F; Figure S4I). Along these lines, *NR4A1*, the key transcription factor responsible for CD16^{hi} CD14^{lo} non-classical monocyte differentiation,⁴³ was prominently expressed in tMonos (Figure 5G).

Next, we assessed tMono phenotypes in more detail. All major tMono subsets exhibited strong expression of neutrophil chemoattractants, i.e., *CXCL8*, *CXCL2*, *CXCL5*, *CXCL3*, and macrophage migration inhibitory factor (*MIF*) (Figure 5G). In addition, transcripts associated with thrombus resolution and recanalization: urokinase receptor, thrombomodulin, VEGF A or B, and tissue factor pathway inhibitor (*PLAUR*, *THBD*, *VEGFA*, *VEGFB*, and *TFPI*), were highly expressed across all major tMono

subsets, most prominently by CXCR4^{hi} cluster 4, as well as THBS1^{high} cluster 3 and CLEC5A^{hi} cluster 0 tMonos (Figure 5G; Figure S4G). Also, tMonos, particularly CXCR4^{hi} cluster 4, expressed high amounts of HIF1-AS3. Multiple cathepsins were enriched in CTSD^{hi} (encoding cathepsin D) cluster 7, suggesting a role of this cluster in extracellular matrix degradation as well as lysosomal protein digestion (Figure 5G). The CTSD^{hi} cluster 7 also showed prominent upregulation of apolipoprotein C-I (APOC1), which is activated when monocytes transdifferentiate to macrophages⁴⁴ (Figure 5G). tMono s exhibited distinct phenotypes while sharing (1) a non-classical monocyte phenotype, (2) clot-resolving features, and (3) expression of neutrophil-attracting factors. Next, we asked if these features were indeed jointly regulated across monocytes in the sense of directed cellular programs. To this end, we employed weighted gene correlation network analysis (WGCNA) to distill coordinative cellular responses as condensed *gene modules*.^{45,46} WGCNA analysis revealed a total of 8 modules of varying size (Figure 5H; Figures S4J and S5). Modules 3–6 were enriched in monocytes within the thrombus (Figures 5H and 5I; Figures S4J and S5) with module 3 depicting the most prominent enrichment within thrombi. Module 3 consisted of neutrophil chemoattracting (MIF), thrombus resolving (PLAUR and THBD), as well as non-classical monocyte defining genes (FCGR3A). This indicates a possible joint upstream regulation of the phenotypic shift in tMonos (Figures 5H and 5I). In summary, tMonos are defined by distinct clusters mainly showing a non-classical-like phenotype with parallel upregulation of neutrophil-chemotactic signals and thrombus-modulating properties.

Reverse translation confirms tMono-driven continuous influx of subsequently pro-resolving neutrophils into thrombi

To allow a detailed understanding of the intercellular immune-cell communication within thrombi, a single-cell interactome analysis was performed on human thrombus and blood immune cells (based on the immune subsets defined in Figure S2B). In line with the strong expression of neutrophil-active chemokines by monocytes, the chemokine interactome outlined abundant intercellular communication pathways between monocyte and neutrophil subsets, strongly mediated by the CXCL8-CXCR1 or CXCL8-CXCR2 axis (Figures 6A; Figures S6A–S6C).

To investigate this concept of dynamic pro-resolving monocyte-neutrophil axes further, we again utilized our established murine inferior vena cava stenosis and *in vitro* thrombosis models. First, we added a characterization of our thrombosis models: scRNA-seq analysis of the thrombosis mouse model confirmed these strong phenotypic shifts in thrombus immune cells compared with circulating innate immune cells (Figures S6D–S6F), hence mimicking low-flow thrombus formation in the left atrial appendage at the single-cell level.^{1,3,4} The presence of thrombosis did not yield any major changes in the circulating immune-cell compartment (Figure 6B). In this murine thrombosis model, monocytes underwent similar phenotypic changes as their human counterparts: again, several neutrophil chemoattractants, including *Cxcl2*, *Ccl2*, *Mif*, *Cxcl16*, and the cytokine *Il1b*, were enriched in tMonos (Figure S6G). A prominent *Ccr2*^{hi} subset (cluster 9) and a smaller *Cx3cr1*^{hi} subset (cluster 14) were present in blood as well as in thrombus (Figures S6D–

S6F). *Ly6c2* (encoding lymphocyte antigen 6 family member C2) was strongly downregulated in the major tMono subset (cluster 9). This corresponded to the phenotypic shift toward a non-classical-like CD16 (FCGR3A)^{high} phenotype observed in human thrombi (Figures S6D–S6G).⁴⁷ Distinct expression patterns of neutrophil chemoattractants and pro-resolving features correlated between murine and human tMonos (Figures S6D–S6J). Employing label transfer confirmed a *Vegfa*^{hi} neutrophil subset in murine neutrophils (Figures S6J and S6K), indicating that the murine disease model mimics the human counterpart.

In addition, differential expression analysis of our *in vitro* model (Figures S2I and S2J) revealed similar differential expression patterns in monocytes and neutrophils: a neutrophil-chemoattractive tMono subset as well as a pro-resolving neutrophil program dominated the landscape of *in vitro* artificially generated human thrombosis (Figures S6L and S6M), suggesting a suitable model for further studying thromboinflammation *in vitro*. However, the changes observed in the *in vitro* system did not completely phenocopy the thrombus formed within the human body: for example, T cells or monocytes in the artificial thrombus showed overall phenotypic and quantitative shifts in the UMAP of the real *in situ* thrombus that were distinct from the artificial *ex vivo* thrombus, indicating that intravital factors (i.e., endotheliopathy or atrial dysfunction) also influence immune-cell phenotype, which cannot fully be copied by *in vitro* models (Figures S2I and S2J).

Based on this prominent neutrophil-chemotactic phenotype of tMonos and the presence of heterogeneous neutrophil populations within thrombi, we hypothesized that the tMono and neutrophil landscape might continuously shift. Indeed, the observed changes in monocyte and neutrophil phenotypes as well as the upregulation of pro-resolving gene expression patterns followed gradual, dynamic cellular shifts rather than a rapid phenotype switching in the *in vitro* thrombosis model (Figures S6N and S6O). Since this *in vitro* model represents a *sealed* system, this confirmed that CD16^{lo} neutrophils and CD16^{hi} monocytes develop from their original CD16^{hi} neutrophil and CD16^{lo} monocyte precursors, as no CD16^{lo} neutrophils and CD16^{hi} monocytes could enter the sealed system. Hence, as short-lived cells, in the setting of thrombosis, CD16^{lo} tNeutros might be at hyperactivated, pre-terminal stages developing from their CD16^{hi} precursors. Similarly, this has been discussed for non-classical monocytes, developing from classical precursors.⁴⁸

Based on the monocyte-neutrophil cross-communication identified in the scRNA-seq, we next hypothesized the possibility of a continuous blood neutrophil recruitment toward established thrombi—mediated by tMonos—allowing steady replenishment of the CD16^{hi} (and subsequent CD16^{lo}) neutrophil population. Therefore, we employed a neutrophil fate-mapping approach in our flow-reduction-induced murine thrombosis model, allowing investigation of the temporal dynamics of neutrophil recruitment. We made use of a multi-color labeling approach—the first surge of neutrophils was labeled with a green-fluorescent antibody (1st wave neutrophils). 48 h after the first labeling, neutrophils were labeled again with a red fluorescent dye (2nd wave neutrophils), allowing differentiation between the first and second surge of neutrophils into the thrombus at 72 h after thrombus induction (sacrifice and organ harvesting) (Figure 6C). Within the

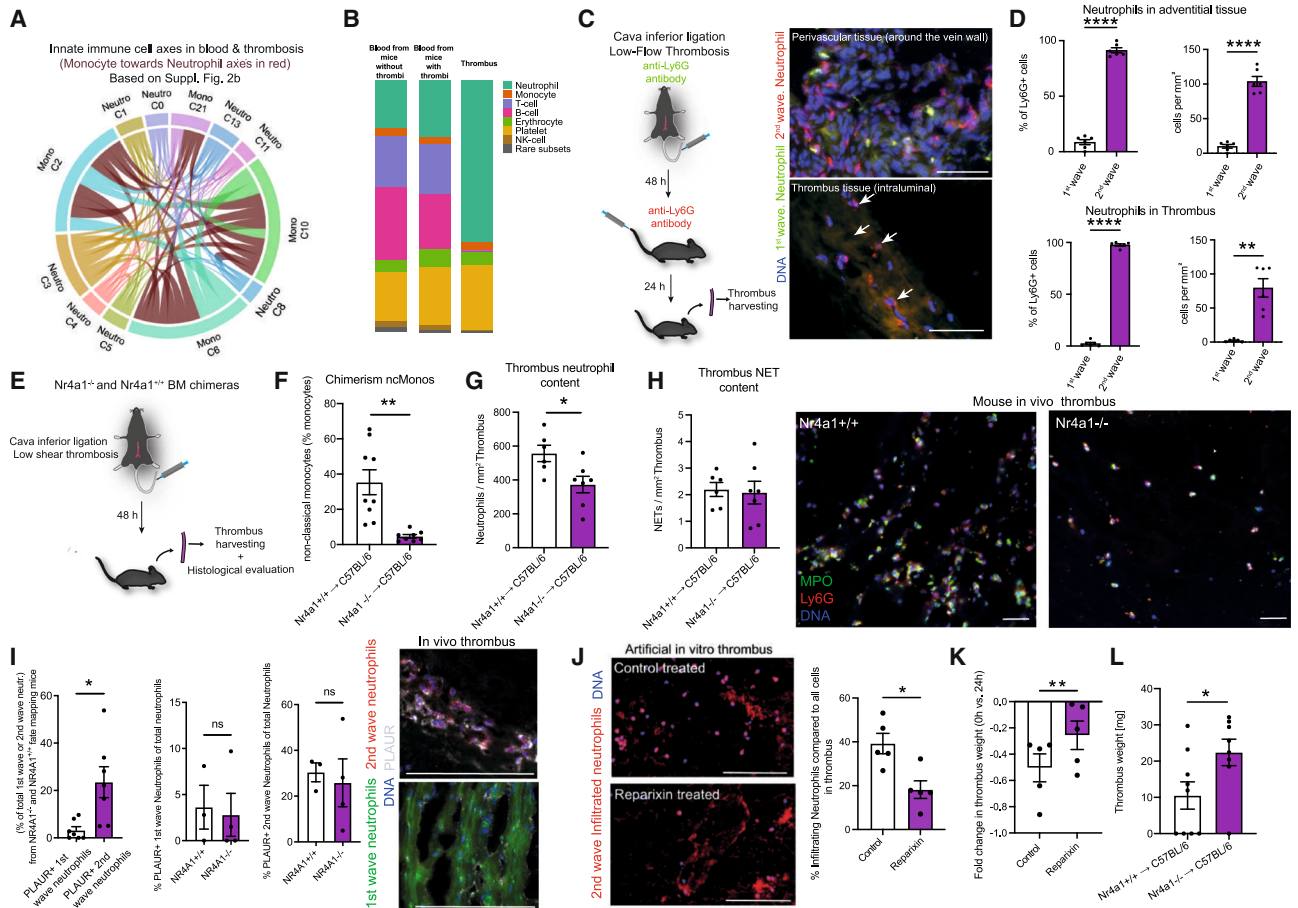


Figure 6. Reverse translation confirms non-classical-like tMonos to fuel continuous blood neutrophil recruitment, resolving thrombosis

(A) Chemokine interactome between human neutrophils and monocytes analyzed for clusters further specified in Figure S2B from the scRNA-seq data. The connections in red highlight monocyte → neutrophil interactions.

(B) Cluster frequencies (with the same color code as the clusters in UMAP) as separated by origin are shown for thrombi as well as blood from mice with thrombi or blood from mice without thrombi, as illustrated in bar plots.

(C) Left: murine model of thrombosis. Illustration depicting the experimental setup: fluorescein isothiocyanate (FITC)-tagged anti-Ly6G neutrophil antibody was injected during inferior vena cava ligation. 48 h after inferior vena cava ligation, PE-tagged anti-Ly6G antibody was injected. 24 h after the second antibody injection, mice were sacrificed, and thrombi were harvested and analyzed histologically. Right: representative epifluorescence images (from $n = 6$ mice) of 1st wave neutrophils (green) and 2nd wave neutrophils (red) and DNA (blue) within the thrombus and within the perivascular tissue. Scale bar: 50 μm .

(D) Quantification of 1st and 2nd wave neutrophils in % of all neutrophils and as cells/ μm^2 in the vessel wall (top) and within the thrombus (bottom). $n = 6$ mice.

(E) Illustration depicting the experimental setup: cava inferior ligation was performed to induce thrombosis by flow reduction. 48 h after flow reduction, chimeric mice were sacrificed, and thrombi were harvested and histologically analyzed.

(F) Analysis of chimerism in $Nr4a1^{-/-}$ mice by determining LY6G^{low} non-classical monocyte counts in blood by flow cytometry. $n = 8-9$ mice.

(G) tNeuro counts per mm^2 in $Nr4a1^{-/-}$ and $Nr4a1^{+/+}$ bone marrow chimeras. $n = 6-7$ mice.

(H) Left: thrombus NET content per mm^2 . $n = 6-7$ mice. Right: representative epifluorescence image of Ly6G⁺ MPO⁺ neutrophils in $Nr4a1^{-/-}$ and $Nr4a1^{+/+}$ bone marrow chimera thrombi. $n = 6-7$ mice. Scale bar: 50 μm .

(I) Quantification on the left: quantification of 1st wave (left), 2nd wave (middle) neutrophils in thrombi from $Nr4a1^{-/-}$ versus $Nr4a1^{+/+}$ bone marrow chimera mice and quantification of 1st versus 2nd wave neutrophils in thrombi pooled from $Nr4a1^{-/-}$ and $Nr4a1^{+/+}$ bone marrow chimera mice (right). Images on the right: 1st wave neutrophils (green), 2nd wave neutrophils (red), DNA (blue), and PLAUR expression (gray) in a $Nr4a1^{+/+}$ WT thrombus, based on the experimental model explained in (C). Scale bar: 125 μm .

(J) Left: representative images (blood and artificial thrombi from $n = 5$ individuals) from immunofluorescence stainings of artificial thrombi embedded into fluorescently labeled neutrophil-rich medium, allowing quantification of secondary neutrophil infiltration (infiltrated neutrophils in red) under control (left image) and reparixin treatment (right image) conditions. Right: quantification of infiltrating neutrophils (compared with all cells) under control or reparixin treatment conditions. Blood and artificial thrombi from $n = 5$ individuals. Scale bar: 100 μm .

(K) Quantification of the fold change in thrombus weight reduction compared with the original thrombus weight (0 versus 24 h) in control or reparixin-treated thrombi. Blood and artificial thrombi from $n = 5$ individuals.

(L) Thrombus weight analysis of $Nr4a1^{-/-}$ and $Nr4a1^{+/+}$ bone marrow chimera thrombi in mg. $n = 8-9$ mice. Paired t test was used for paired, normally distributed data. Unpaired t test was used for normally distributed and unpaired data, and Mann-Whitney test was used for non-parametrically distributed data. * $p < 0.05$. ** $p < 0.01$. This figure is also related to Figure S6.

perivascular tissue, a green and a red fluorescing neutrophil population were detectable, indicating a successful fate-mapping approach (Figure 6C). In thrombi, 1st wave neutrophils (present during the early formation of thrombi) were rarely detectable, but 2nd wave neutrophils (infiltrated after thrombi had already formed) were present at high frequencies. This might indicate that neutrophils infiltrate the thrombus also at later stages, continuously replacing short-lived earlier tNeutro populations, which might no longer be detectable due to NETosis¹ (Figure 6D). Next, based on the human scRNA-seq data, we hypothesized that human CD16 (FCGR3A)^{hi} monocytes, corresponding to murine *Ly6c*^{lo} monocytes, substantially fuel this continuous tNeutro influx by their above-mentioned prominent expression of neutrophil chemoattractants.

The transcription factor NR4A1 essentially mediates the transition toward a *Ly6c*^{lo} monocyte phenotype,⁴³ thereby providing a tool for genetic depletion of non-classical tMonos. We used *Nr4a1*^{-/-} bone marrow chimeras to assess the contribution of tMonos to neutrophil accumulation within thrombi (Figure 6E). In line, genetic deletion of *Nr4a1* in bone marrow-derived cells depletes non-classical monocytes as described.⁴⁹ Flow cytometric analysis confirmed a depletion of circulating *Ly6c*^{lo} monocytes (Figure 6F; Figure S6P). The flow-reduction vena cava stenosis model of thrombosis in these mice showed a reduced neutrophil content in thrombi from *Nr4a1*^{-/-} chimeras compared with control chimeras without any changes in NET content, confirming *Nr4a1*^{hi} non-classical-like monocytes to—at least in part—drive neutrophil influx into thrombi (Figures 6G and 6H). 2nd wave neutrophils showed PLAUR expression more frequently compared with 1st generation neutrophils; however, the distribution of PLAUR⁺ 1st versus 2nd wave neutrophils remained unchanged in chimeric *Nr4a1*^{-/-} thrombi compared with *Nr4a1*^{+/+} chimeras (Figure 6I). Hence, in monocyte-mediated neutrophil attraction, later waves of infiltrating neutrophils indeed showed PLAUR expression more frequently than the early wave of neutrophils, indicating a more pro-resolving function of these (non-classical monocyte attracted) 2nd wave neutrophils compared with neutrophils participating in thrombus initiation. *In vitro*, inhibition of the CXCL8-signaling axis (CXCR1 and CXCR2) by Reparixin indeed resulted in a reduced infiltration of external neutrophils into established thrombi and diminished thrombus resolution (Figures 6J and 6K). In line, *in vivo*, the impaired neutrophil infiltration into thrombi in *Nr4a1*^{-/-} chimeras correlated with an increased thrombus weight (Figure 6L).

Assessment of clotting or clot formation time, maximum clot firmness, and maximum lysis by thrombelastometry (TEG) excluded a significant direct difference in coagulation between *Nr4a1*^{-/-} chimeras and wild-type (WT) mice *in vitro* (Figure S6Q). TEG measures acute *in vitro* thrombus formation without subsequent processes such as enrichment of non-classical-like monocyte or neutrophil recruitment. Also, TEG only measures the very first steps of thrombus formation in a short time frame, not capturing changes that occur within hours after thrombus formation, i.e., *Nr4a1*-dependent changes. Hence, this underlines possible indirect effects of non-classical-like monocytes by recruiting neutrophils *in vivo* during the thrombus resolution phase.

In summary, this study provides reverse translational evidence for the functional importance of the phenotypic shifts and inter-

cellular communication axes within the innate immune compartment as observed by multi-omic measures into comparable *in vivo* and *in vitro* models. These models unravel unexpected pro-resolving monocyte-neutrophil axes fueled by *Nr4a1*^{hi} tMonocytes, continuously recruiting blood-borne neutrophils into the thrombus, which become hypoxic and subsequently polarize into thrombolytic and angiogenic tNeutros.

DISCUSSION

The contribution of immune cells to thrombosis has become a center of attention in multiple diseases beyond cardiovascular disease, particularly in COVID-19, but also in autoimmunity, sepsis, and cancer.^{1,50,51} The importance of immune cells to thrombosis has been extensively studied in animal models in the past decades, deeming innate immune cells strongly pro-thrombotic at early phases of thrombogenesis.^{1,4} However, translational approaches that allow a cellular and functional understanding of the immune landscape in human thrombosis have been lacking. The exact leukocyte phenotypes during thrombotic transition in respect to classical blood phenotypes remained unclear. We hypothesized that after thrombus formation in established clots, immune-cell axes might not be purely pro-thrombotic, challenging the concept of sole detrimental thromboinflammation. Indeed, we found functionally heterogeneous neutrophils and monocytes as the most enriched leukocyte subsets within human thrombi. Simultaneously, neutrophils and monocytes—unlike NK cells, T cells, or B cells—underwent strong phenotypic shifts in thrombi compared with their blood counterparts, as evidenced by the transcriptome and surfaceome. Velocity analysis, as well as *in vitro* assays, suggested that these neutrophil and monocyte subsets might emerge from continuous shifts from distinct blood precursors. We revealed that intercommunicating neutrophil and monocyte subsets held highly specialized thromboinflammatory and immunothrombolytic features in humans and mice. Concretely, tMonos formed a heterogeneous tMono landscape, which was characterized by its CD16^{hi} NR4A1^{hi} phenotype with strong neutrophil-chemoattracting features across all tMono subsets. Simultaneously, tMonos, in contrast to circulating blood monocytes, showed pronounced thrombus-modulating properties with different cluster-specific functions. Monocyte cluster 3 held strong thrombolytic and pro-resolving properties with high THBD, PLAUR, and THBS1 expression. Whereas tMono cluster 7 showed high expression of FN1 and cathepsins, both associated with thrombus formation.^{34,35,52,53} A weighted gene co-expression network analysis suggested these monocyte programs to be regulated in a joint, upstream manner across single cells. However, coagulation activation, but not hypoxia per se, recapitulated this non-classical monocyte phenotype *in vitro*, which points toward monocyte polarization driven by the thrombus microenvironment. This pro-resolving thrombus alternative monocyte phenotype is in line with previously described vasculoprotective properties of non-classical monocytes.^{54,55}

The human neutrophil landscape in thrombosis is highly diverse, with pro-thrombotic subsets present in blood and within thrombi, enriched in pro-NETotic genes and with cellular states such as PADI4 associated with NETosis and an aberrant activation of host defense as seen in immunothrombosis.⁵⁶ On the

other hand, a very prominent pro-resolving neutrophil subset is confined to thrombi and not present in the circulating neutrophil landscape (VEGFA^{hi} cluster 2 neutrophils). This VEGFA^{hi} neutrophil subset is functionally reminiscent yet transcriptionally distinct from previously described proangiogenic neutrophils.⁵⁷ In addition to pro-resolving PLAUR, PLAU, VEGFA, and VEGFB, the neutrophil cluster 2 was particularly enriched in hypoxia-driven HIF1A-AS3. Indeed, this distinct phenotype of neutrophil cluster 2 can be reproduced by pharmacological hypoxia induction. In earlier mouse studies, HIF1 α —also induced upon HIF1 α stimulation—correlated negatively with oxygen tension in the thrombus but positively with *Vegfa* expression.^{58,59} Augmenting local physiological immune-thrombolytic pathways might hence facilitate effective thrombolysis without triggering major systemic side effects. *In vivo* genetic deletion of HIF1 α in myeloid leukocytes in a mouse model of thrombosis by flow restriction resulted in exacerbation of thrombosis burden and reduced the frequency of PLAUR⁺ pro-resolving neutrophils.

Indeed, *in vitro* hypoxia mimicking by roxadustat induced a shifting between CD16^{hi} to CD16^{lo} neutrophil spectra—also observed in tNeutros—and induced a pro-resolving phenotype. CD16 on neutrophils has been described as a maturation as well as an apoptosis marker and associated with inflammatory activation or myeloid malignancies. Furthermore, the loss of CD16 expression has been associated with low density and a prolonged neutrophil survival.^{23–26} In the setting of thrombosis, CD16^{lo} tNeutros might be at hyperactivated, pre-terminal stages.

Mimicking human low-flow thrombosis, a flow restriction thrombosis model in mice indeed recapitulated human immune-cell composition and phenotype on a single-cell level. This allowed mechanistic analysis and manipulation of the observed monocyte-neutrophil cross-communication. Since tMonos held strong neutrophil-chemoattracting properties, we hypothesized that blood neutrophils might continuously infiltrate the thrombus.

An *in vivo* fate-mapping approach upon flow-reduction-induced thrombosis indeed suggested neutrophils to continuously infiltrate established thrombi. Depletion of *Nr4a1*^{hi} neutrophil-chemoattractive tMonos reduced this tNeuro influx and led to exacerbation of thrombus burden in mice *in vivo*. Depletion of the CXCL8-CXCR1/2 axis reduced neutrophil infiltration into human *in vitro* thrombi and again related to an increased thrombus burden. This suits the neutrophil-attracting properties described for *Nr4a1*-dependent *Ly6c*^{lo} monocytes⁴³ and their contribution to vascular homeostasis under physiological conditions: scavenging endothelial debris in the vasculature.²² This is in line with early reports on thrombus resolution upon *in vivo* interleukin-8 administration¹⁴ and an impaired thrombus resolution during neutropenia.⁶⁰

VEGFA^{hi} neutrophils strongly upregulate the plasminogen activator urokinase within the thrombotic environment. Urokinase as well as other plasminogen activators are most efficiently being used by neurologists to treat ischemic strokes and rapidly restore cerebral blood flow, but these are accompanied by significant systemic bleeding risks.^{61,62} An intrinsic thrombolytic phenotype of distinct neutrophils, characterized by upregulation of these classical clinically used therapeutic agents, might outline intrinsic thrombus-resolving properties by thrombus leu-

kocytes. Therefore, this identifies the therapeutic manipulation of immune cells, phenocopying distinct thrombolytic immune phenotypes, as an option to support local thrombolysis without risking bleeding side effects. Importantly, however, extensive further cellular and molecular bioengineering approaches and mechanistic follow-up studies will be required to investigate and exploit the complete relevance and potential cell-specific therapeutic opportunities provided by this single-cell immune landscape of thrombosis.

In summary, this study maps the immune landscape of thrombo-inflammation, provides a resource for future research in vascular immunology, and benchmarks highly specialized immune-cell phenotypes that underline the plasticity of immune cells in resolving vascular disease. Beyond the descriptive multi-omics approach, the presence of a pro-resolving *Nr4a1*-driven monocyte-neutrophil axis in mechanistic follow-up analyses—closely resembling the human counterpart—further supports key multi-omic deduced cellular axes and pro-resolving effects at a mechanistic level: blood neutrophils are continuously recruited to *in vitro* and *in vivo* thrombi and acquire a HIF1 α -mediated pro-resolving phenotype that promotes resolution of thrombosis. This is fueled by pro-resolving and neutrophil-chemoattractive thrombus non-classical monocytes.

Disruption of this monocyte-neutrophil axis by depletion of either (1) *Nr4a1*^{hi} monocytes *in vivo* or (2) the culprit cross-communication CXCL8-CXCR1 or CXCL8-CXCR2 axis *in vitro* results in reduced neutrophil influx and exacerbated thrombus burden. Along these lines, (3) induction of HIF1 α signaling in neutrophils *in vitro* facilitates thrombolysis, and, by contrast, (4) deleting HIF1 α signaling in myeloid leukocytes *in vivo* culminates in fewer PLAUR⁺ neutrophils in thrombi and an exacerbation of thrombosis burden.

This describes so far unknown neutrophil and monocyte phenotypes, which hold important ramifications for immune-cell plasticity, acquiring protective roles in the context of resolving deadly thrombotic events, which we term immunothrombolysis. Further, this dataset holds important directions for future research on the immunologic aspect of thrombosis, outlining multiple thrombolytic but also pro-thrombotic immune-cell phenotypes as possible therapeutic targets that might allow circumvention of increased bleeding risks in conventional therapies.^{1,2,63}

Limitations

This study holds limitations. First, human thromboemboli are highly heterogeneous: for example, risk factors, comorbidities, clot origin, medication, patient and thrombus age, and gender might influence immune phenotypes. This study was not designed to resolve differences in thrombus compositions induced by different influencing clinical variables. Importantly, the employed thrombosis models only represent approximations, and further mechanistic investigations are required to validate the concept of immunothrombolysis. In addition, different omic approaches hold different downsides, as for example (1) platelets, platelet-leukocyte aggregates, or pre-terminal immune-cell substates cannot sufficiently be captured by scRNA-seq approaches, and hence different leukocyte subsets cannot be plainly compared in-between omic approaches; (2) cells might be subjected to artificial shifts; and (3) the complete heterogeneity of cellular subsets cannot be isolated and

validated in mechanistic assays within a single study. Last but not least, distinct differences in cellular composition might exist between venous-derived blood leukocytes and artery-occluding thromboemboli.

RESOURCE AVAILABILITY

Lead contact

The lead contact is Kami Pekayvaz (kami.pekayvaz@med.uni-muenchen.de). The lead contact will answer to material, data, and code availability requests.

Materials availability

The materials are available upon request from the corresponding authors.

Data and code availability

The sequencing data and source code are available at Zenodo: <https://doi.org/10.5281/zenodo.10466853>.

ACKNOWLEDGMENTS

This study was supported by the ERC-Starting grant “T-MEMORE” (ERC grant 947611 [K.S.]) and the ERC-Advanced grant “IMMUNOTHROMBOSIS” (ERC-2018-ADG [S.M.]). Further, the project was supported by Deutsche Herzstiftung e.V., Frankfurt a.M. (K.P. and L.N.), the Else-Kröner-Fresenius Stiftung (K.P.), DZHK Postdoc Start-up Grant (K.P.), DZHK Säule B Antrag DZHK B 21-014 SE (K.P. and L.N.), the DZHK Junior Research Group fellowship—funding code 81X3600233 (K.P.), the Corona Foundation (L.N.), the Deutsche Forschungsgemeinschaft (DFG) SFB 914 (S.M. [B02 and Z01], K.S. [B02]), the DFG SFB 1123 (S.M., L.N., and B.E. [B06]; K.S. [A07]; and M.J. and R.Z. [Z02]), the DFG SFB TR359 (K.S. [A03]), the DFG SFB1321 (B.E. [P10] and S.M. [P10]), the DFG FOR 2033 (S.M.), the DFG SFB1243 (W.E. [A14]), the DFG EN 1093/2-1 (W.E. and A.J.), LMUexcellent (K.P.), the DFG Clinician Scientist program PRIME (413635475, K.P. and R.K.), and the German Centre for Cardiovascular Research (DZHK) (Clinician Scientist Programme [L.N.], MHA 1.4VD [S.M.], and DZHK partner site project [K.S.]). S.T. received grants from the Corona Foundation, the Leducq Foundation, the Medical and Clinician Scientist Program of the LMU Medical Faculty, and the European Joint Programme for Rare Diseases. Graphical abstract created in BioRender. <https://BioRender.com/26vctqm>.

AUTHOR CONTRIBUTIONS

Conception, experimental design, project administration, and supervision: K.P., L.N., and K.S.; writing – original draft: K.P.; patient identification, patient information and informed consent acquisition, and sample acquisition: N.M., M.R.H.P., K.P., K.S., L.N., T.B.-B., T.L., and S.T.; methodology, investigation, and formal analysis: K.P., B.K., L.N., S.A., K.Y., H.S., L.B., T.T.M., L.H., S.M., S.W., J.F., A.T., M.J., S.B., V.K., L.E., A.M.-N., R.K., N.M., S.S., A.J., V.P., A.D.z.S., and M.V.; writing & editing: all authors; visualization: K.P., A.L., and M.J.; funding acquisition: K.P., S.T., M.D., B.E., R.Z., S.M., L.N., and K.S.

DECLARATION OF INTERESTS

L.N. and K.P. received the Bayer Thrombosis Research Award in 2023 and 2025.

STAR★METHODS

Detailed methods are provided in the online version of this paper and include the following:

- KEY RESOURCES TABLE
- EXPERIMENTAL MODEL AND STUDY PARTICIPANT DETAILS
 - Ethics and patient cohort
 - Deep vein thrombosis - Mouse model of flow restriction in the IVC
 - Intravital neutrophil fate mapping
 - Bone marrow transplant

METHOD DETAILS

- Single-cell preparation and flow-cytometry
- RT-PCR of isolated neutrophils from young versus older thrombi
- Thrombus clearance by Roxadustat-stimulated neutrophils
- scRNA-seq of real and artificial (*in vitro* generated) thrombus
- Preparation for prime-seq RNAseq of blood and thrombus neutrophils and monocytes
- prime-seq
- ScRNA-seq of human and mouse blood and thrombi
- CITE-Seq
- Bioinformatic analysis of prime-seq data
- Differential Gene Expression Analysis
- Overrepresentation analysis
- scRNAseq data analysis
- Chemokine interactome analysis
- scVelo
- Monocle3 analysis
- Label transfer human and mouse neutrophils
- Neutrophil and PBMC isolation and pharmacological hypoxia mimicking
- Artificial coagulation activation and subsequent monocyte analysis
- *In vitro* fibrin clearance by CD16^{low} and CD16^{high} neutrophils
- Flow cytometry of thrombus neutrophils and monocytes at different timepoints after artificial thrombus induction
- Flow cytometry of Roxadustat-stimulated neutrophils
- Flow Cytometry Sort, staining and microscopy of neutrophils and monocytes from artificial thrombi
- Immunofluorescence staining and quantification of thrombus neutrophils in mouse thrombi
- Immunohistochemical analyses in human FFPE or fresh frozen thrombi
- Neutrophil infiltration and thrombus regression upon Reparixin or control treatment in artificial thrombi
- ROTEM Analysis

QUANTIFICATION AND STATISTICAL ANALYSIS

- Quantification and statistical analysis

SUPPLEMENTAL INFORMATION

Supplemental information can be found online at <https://doi.org/10.1016/j.immuni.2025.03.020>.

Received: August 30, 2024

Revised: December 31, 2024

Accepted: March 27, 2025

Published: April 24, 2025

REFERENCES

1. Stark, K., and Massberg, S. (2021). Interplay between inflammation and thrombosis in cardiovascular pathology. *Nat. Rev. Cardiol.* 18, 666–682. <https://doi.org/10.1038/s41569-021-00552-1>.
2. Freedman, B., Potpara, T.S., and Lip, G.Y.H. (2016). Stroke prevention in atrial fibrillation. *Lancet* 388, 806–817. [https://doi.org/10.1016/S0140-6736\(16\)31257-0](https://doi.org/10.1016/S0140-6736(16)31257-0).
3. Stark, K., Philippi, V., Stockhausen, S., Busse, J., Antonelli, A., Miller, M., Schubert, I., Hoseinpour, P., Chandraratne, S., von Brühl, M.L., et al. (2016). Disulfide HMGB1 derived from platelets coordinates venous thrombosis in mice. *Blood* 128, 2435–2449. <https://doi.org/10.1182/blood-2016-04-710632>.
4. von Brühl, M.L., Stark, K., Steinhart, A., Chandraratne, S., Konrad, I., Lorenz, M., Khandoga, A., Tirniceriu, A., Coletti, R., Köllnberger, M., et al. (2012). Monocytes, neutrophils, and platelets cooperate to initiate and propagate venous thrombosis in mice *in vivo*. *J. Exp. Med.* 209, 819–835. <https://doi.org/10.1084/jem.20112322>.
5. Duerschmied, D., Suidan, G.L., Demers, M., Herr, N., Carbo, C., Brill, A., Cifuni, S.M., Mauler, M., Cicko, S., Bader, M., et al. (2013). Platelet

- serotonin promotes the recruitment of neutrophils to sites of acute inflammation in mice. *Blood* 121, 1008–1015. <https://doi.org/10.1182/blood-2012-06-437392>.
6. Wang, Y., Gao, H., Shi, C., Erhardt, P.W., Pavlovsky, A., A Soloviev, D., Bledzka, K., Ustinov, V., Zhu, L., Qin, J., et al. (2017). Leukocyte integrin Mac-1 regulates thrombosis via interaction with platelet GPIIb/IIIa. *Nat. Commun.* 8, 15559. <https://doi.org/10.1038/ncomms15559>.
 7. Marx, C., Novotny, J., Salbeck, D., Zellner, K.R., Nicolai, L., Pekayvaz, K., Kilani, B., Stockhausen, S., Bürgener, N., Kupka, D., et al. (2019). Eosinophil-platelet interactions promote atherosclerosis and stabilize thrombosis with eosinophil extracellular traps. *Blood* 134, 1859–1872. <https://doi.org/10.1182/blood.2019000518>.
 8. Gupta, N., Sahu, A., Prabhakar, A., Chatterjee, T., Tyagi, T., Kumari, B., Khan, N., Nair, V., Bajaj, N., Sharma, M., et al. (2017). Activation of NLRP3 inflammasome complex potentiates venous thrombosis in response to hypoxia. *Proc. Natl. Acad. Sci. USA* 114, 4763–4768. <https://doi.org/10.1073/pnas.1620458114>.
 9. Stark, K., Kilani, B., Stockhausen, S., Busse, J., Schubert, I., Tran, T.D., Gaertner, F., Leunig, A., Pekayvaz, K., Nicolai, L., et al. (2024). Antibodies and complement are key drivers of thrombosis. *Immunity* 57, 2140–2156.e10. <https://doi.org/10.1016/j.immuni.2024.08.007>.
 10. Riegger, J., Byrne, R.A., Joner, M., Chandraratne, S., Gershlick, A.H., Ten Berg, J.M., Adriaenssens, T., Guagliumi, G., Godschalk, T.C., Neumann, F.J., et al. (2016). Histopathological evaluation of thrombus in patients presenting with stent thrombosis. A multicenter European study: a report of the prevention of late stent thrombosis by an interdisciplinary global European effort consortium. *Eur. Heart J.* 37, 1538–1549. <https://doi.org/10.1093/eurheartj/ehv419>.
 11. Xu, R.G., and Ariens, R.A.S. (2020). Insights into the composition of stroke thrombi: heterogeneity and distinct clot areas impact treatment. *Haematologica* 105, 257–259. <https://doi.org/10.3324/haematol.2019.238816>.
 12. Savchenko, A.S., Martinod, K., Seidman, M.A., Wong, S.L., Borissoff, J.I., Piazza, G., Libby, P., Goldhaber, S.Z., Mitchell, R.N., and Wagner, D.D. (2014). Neutrophil extracellular traps form predominantly during the organizing stage of human venous thromboembolism development. *J. Thromb. Haemost.* 12, 860–870. <https://doi.org/10.1111/jth.12571>.
 13. Novotny, J., Oberdieck, P., Titova, A., Pelisek, J., Chandraratne, S., Nicol, P., Hapfelmeier, A., Joner, M., Maegdefessel, L., Poppert, H., et al. (2020). Thrombus NET content is associated with clinical outcome in stroke and myocardial infarction. *Neurology* 94, e2346–e2360. <https://doi.org/10.1212/WNL.0000000000009532>.
 14. Henke, P.K., Wakefield, T.W., Kadell, A.M., Linn, M.J., Varma, M.R., Sarkar, M., Hawley, A., Fowlkes, J.B., and Strieter, R.M. (2001). Interleukin-8 administration enhances venous thrombosis resolution in a rat model. *J. Surg. Res.* 99, 84–91. <https://doi.org/10.1006/jsre.2001.6122>.
 15. Pekayvaz, K., Gold, C., Hoseinpour, P., Engel, A., Martinez-Navarro, A., Eivers, L., Coletti, R., Joppich, M., Dionisio, F., Kaiser, R., et al. (2023). Mural cell-derived chemokines provide a protective niche to safeguard vascular macrophages and limit chronic inflammation. *Immunity* 56, 2325–2341.e15. <https://doi.org/10.1016/j.immuni.2023.08.002>.
 16. Pekayvaz, K., Losert, C., Knottenberg, V., Gold, C., van Blokland, I.V., Oelen, R., Groot, H.E., Benjamins, J.W., Brambs, S., Kaiser, R., et al. (2024). Multiomic analyses uncover immunological signatures in acute and chronic coronary syndromes. *Nat. Med.* 30, 1696–1710. <https://doi.org/10.1038/s41591-024-02953-4>.
 17. Cao, J., Spielmann, M., Qiu, X., Huang, X., Ibrahim, D.M., Hill, A.J., Zhang, F., Mundlos, S., Christiansen, L., Steemers, F.J., et al. (2019). The single-cell transcriptional landscape of mammalian organogenesis. *Nature* 566, 496–502. <https://doi.org/10.1038/s41586-019-0969-x>.
 18. Fernandez, D.M., Rahman, A.H., Fernandez, N.F., Chudnovskiy, A., Amir, E.D., Amadori, L., Khan, N.S., Wong, C.K., Shamailova, R., Hill, C.A., et al. (2019). Single-cell immune landscape of human atherosclerotic plaques. *Nat. Med.* 25, 1576–1588. <https://doi.org/10.1038/s41591-019-0590-4>.
 19. Gong, Y., and Koh, D.R. (2010). Neutrophils promote inflammatory angiogenesis via release of preformed VEGF in an in vivo corneal model. *Cell Tissue Res.* 339, 437–448. <https://doi.org/10.1007/s00441-009-0908-5>.
 20. Janjic, A., Wange, L.E., Bagnoli, J.W., Geuder, J., Nguyen, P., Richter, D., Vieth, B., Vick, B., Jeremias, I., Ziegenhain, C., et al. (2022). Prime-seq, efficient and powerful bulk RNA sequencing. *Genome Biol.* 23, 88. <https://doi.org/10.1186/s13059-022-02660-8>.
 21. Kaiser, R., Gold, C., Joppich, M., Loew, Q., Akhalkatsi, A., Mueller, T.T., Offensperger, F., Droste zu Senden, A., Popp, O., di Fina, L., et al. (2024). Peripheral priming induces plastic transcriptomic and proteomic responses in circulating neutrophils required for pathogen containment. *Sci. Adv.* 10, ead1710. <https://doi.org/10.1126/sciadv.adl1710>.
 22. Carlini, L.M., Stamatiades, E.G., Auffray, C., Hanna, R.N., Glover, L., Vizcay-Barrena, G., Hedrick, C.C., Cook, H.T., Diebold, S., and Geissmann, F. (2013). Nr4a1-dependent Ly6C(low) monocytes monitor endothelial cells and orchestrate their disposal. *Cell* 153, 362–375. <https://doi.org/10.1016/j.cell.2013.03.010>.
 23. Bzowska, M., Hamczyk, M., Skalniak, A., and Guzik, K. (2011). Rapid Decrease of CD16 (FcγRIII) Expression on Heat-Shocked Neutrophils and Their Recognition by Macrophages. *J. Biomed. Biotechnol.* 2011, 284759. <https://doi.org/10.1155/2011/284759>.
 24. Morrissey, S.M., Geller, A.E., Hu, X., Tieri, D., Ding, C., Klaes, C.K., Cooke, E.A., Woeste, M.R., Martin, Z.C., Chen, O., et al. (2021). A specific low-density neutrophil population correlates with hypercoagulation and disease severity in hospitalized COVID-19 patients. *JCI Insight* 6, e148435. <https://doi.org/10.1172/jci.insight.148435>.
 25. Moulding, D.A., Hart, C.A., and Edwards, S.W. (1999). Regulation of neutrophil FcγRIIIb (CD16) surface expression following delayed apoptosis in response to GM-CSF and sodium butyrate. *J. Leukoc. Biol.* 65, 875–882. <https://doi.org/10.1002/jlb.65.6.875>.
 26. Carulli, G., Gianfaldoni, M.L., Azzara, A., Papeschi, F., Vanacore, R., Minnucci, S., Testi, R., and Ambrogi, F. (1992). FcRIII (CD16) expression on neutrophils from chronic myeloid leukemia. A flow cytometric study. *Leuk. Res.* 16, 1203–1209. [https://doi.org/10.1016/0145-2126\(92\)90120-V](https://doi.org/10.1016/0145-2126(92)90120-V).
 27. Stoeckius, M., Hafemeister, C., Stephenson, W., Houck-Loomis, B., Chattopadhyay, P.K., Swerdlow, H., Satija, R., and Smibert, P. (2017). Simultaneous epitope and transcriptome measurement in single cells. *Nat. Methods* 14, 865–868. <https://doi.org/10.1038/nmeth.4380>.
 28. Chen, T., Li, Y., Sun, R., Hu, H., Liu, Y., Herrmann, M., Zhao, Y., and Muñoz, L.E. (2021). Receptor-Mediated NETosis on Neutrophils. *Front. Immunol.* 12, 775267. <https://doi.org/10.3389/fimmu.2021.775267>.
 29. Sprengeler, E.G.G., Zandstra, J., van Kleef, N.D., Goetschalckx, I., Verstegen, B., Aarts, C.E.M., Janssen, H., Tool, A.T.J., van Mierlo, G., van Bruggen, R., et al. (2022). S100A8/A9 Is a Marker for the Release of Neutrophil Extracellular Traps and Induces Neutrophil Activation. *Cells* 11, 236. <https://doi.org/10.3390/cells11020236>.
 30. Palmer, L.J., Damgaard, C., Holmstrup, P., and Nielsen, C.H. (2016). Influence of complement on neutrophil extracellular trap release induced by bacteria. *J. Periodont. Res.* 51, 70–76. <https://doi.org/10.1111/jre.12284>.
 31. de Bont, C.M., Boelens, W.C., and Puijck, G.J.M. (2019). NETosis, complement, and coagulation: a triangular relationship. *Cell. Mol. Immunol.* 16, 19–27. <https://doi.org/10.1038/s41423-018-0024-0>.
 32. Dou, H., Kotini, A., Liu, W., Fidler, T., Endo-Umeda, K., Sun, X., Olszewska, M., Xiao, T., Abramowicz, S., Yalcinkaya, M., et al. (2021). Oxidized Phospholipids Promote NETosis and Arterial Thrombosis in LNK(SH2B3) Deficiency. *Circulation* 144, 1940–1954. <https://doi.org/10.1161/CIRCULATIONAHA.121.056414>.
 33. Stark, K., Kilani, B., Stockhausen, S., Busse, J., Schubert, I., Thuy-Duong, T., Gaertner, F., Leunig, A., Pekayvaz, K., Nicolai, L., et al. (2024). Antibodies and complement are key drivers of thrombosis. *Immunity* 57, 2140–2156.e10. <https://doi.org/10.1016/j.immuni.2024.08.007>.
 34. Maurer, L.M., Tomasini-Johansson, B.R., and Mosher, D.F. (2010). Emerging roles of fibronectin in thrombosis. *Thromb. Res.* 125, 287–291. <https://doi.org/10.1016/j.thromres.2009.12.017>.

35. Wang, Y., Reheman, A., Spring, C.M., Kalantari, J., Marshall, A.H., Wolberg, A.S., Gross, P.L., Weitz, J.I., Rand, M.L., Mosher, D.F., et al. (2014). Plasma fibronectin supports hemostasis and regulates thrombosis. *J. Clin. Invest.* *124*, 4281–4293. <https://doi.org/10.1172/JCI74630>.
36. Lood, C., Blanco, L.P., Purmalek, M.M., Carmona-Rivera, C., De Ravin, S.S., Smith, C.K., Malech, H.L., Ledbetter, J.A., Elkon, K.B., and Kaplan, M.J. (2016). Neutrophil extracellular traps enriched in oxidized mitochondrial DNA are interferogenic and contribute to lupus-like disease. *Nat. Med.* *22*, 146–153. <https://doi.org/10.1038/nm.4027>.
37. Muller, S., and Radic, M. (2016). Oxidation and mitochondrial origin of NET DNA in the pathogenesis of lupus. *Nat. Med.* *22*, 126–127. <https://doi.org/10.1038/nm.4044>.
38. Takishita, Y., Yasuda, H., Shimizu, M., Matsuo, A., Morita, A., Tsutsumi, T., Tsuchiya, M., and Sato, E.F. (2020). Formation of neutrophil extracellular traps in mitochondrial DNA-deficient cells. *J. Clin. Biochem. Nutr.* *66*, 15–23. <https://doi.org/10.3164/jcbn.19-77>.
39. Yousefi, S., Mihalache, C., Kozlowski, E., Schmid, I., and Simon, H.U. (2009). Viable neutrophils release mitochondrial DNA to form neutrophil extracellular traps. *Cell Death Differ.* *16*, 1438–1444. <https://doi.org/10.1038/cdd.2009.96>.
40. Yipp, B.G., and Kubes, P. (2013). NETosis: how vital is it? *Blood* *122*, 2784–2794. <https://doi.org/10.1182/blood-2013-04-457671>.
41. D’Cruz, A.A., Speir, M., Bliss-Moreau, M., Dietrich, S., Chen, A.A., Gavillet, M., Lawlor, K.E., Vince, J.E., Kelliher, M., Hakem, R., et al. (2018). Padi4 Regulates NET Formation and Inflammatory Cell Death Downstream of Mkl. *Blood* *132*, 276. <https://doi.org/10.1182/blood-2018-99-110051>.
42. Bergen, V., Lange, M., Peidli, S., Wolf, F.A., and Theis, F.J. (2020). Generalizing RNA velocity to transient cell states through dynamical modeling. *Nat. Biotechnol.* *38*, 1408–1414. <https://doi.org/10.1038/s41587-020-0591-3>.
43. Bharat, A., McQuattie-Pimentel, A.C., and Budinger, G.R.S. (2017). Non-classical monocytes in tissue injury and cancer. *Oncotarget* *8*, 106171–106172. <https://doi.org/10.18632/oncotarget.22584>.
44. Liu, H., Shi, B., Huang, C.-C., Eksarko, P., and Pope, R.M. (2008). Transcriptional diversity during monocyte to macrophage differentiation. *Immunol. Lett.* *117*, 70–80. <https://doi.org/10.1016/j.imlet.2007.12.012>.
45. Kazer, S.W., Aicher, T.P., Muema, D.M., Carroll, S.L., Ordovas-Montanes, J., Miao, V.N., Tu, A.A., Ziegler, C.G.K., Nyquist, S.K., Wong, E.B., et al. (2020). Integrated single-cell analysis of multicellular immune dynamics during hyperacute HIV-1 infection. *Nat. Med.* *26*, 511–518. <https://doi.org/10.1038/s41591-020-0799-2>.
46. Pekayvaz, K., Leunig, A., Kaiser, R., Joppich, M., Brambs, S., Janjic, A., Popp, O., Nixdorf, D., Fumagalli, V., Schmidt, N., et al. (2022). Protective immune trajectories in early viral containment of non-pneumonic SARS-CoV-2 infection. *Nat. Commun.* *13*, 1018. <https://doi.org/10.1038/s41467-022-28508-0>.
47. Wolf, A.A., Yáñez, A., Barman, P.K., and Goodridge, H.S. (2019). The Ontogeny of Monocyte Subsets. *Front. Immunol.* *10*, 1642. <https://doi.org/10.3389/fimmu.2019.01642>.
48. Pimenov, L., Gonzalez, A.L., Doran, A.C., and Knapp, S. (2024). Same name, different game?—How ontogeny shapes classical monocyte phenotypes. *Genes Immun.* *25*, 1–3. <https://doi.org/10.1038/s41435-023-00248-1>.
49. Hanna, R.N., Cekic, C., Sag, D., Tacke, R., Thomas, G.D., Nowhyed, H., Herrley, E., Rasquinha, N., McArdle, S., Wu, R., et al. (2015). Patrolling monocytes control tumor metastasis to the lung. *Science* *350*, 985–990. <https://doi.org/10.1126/science.aac9407>.
50. Gu, S.X., Tyagi, T., Jain, K., Gu, V.W., Lee, S.H., Hwa, J.M., Kwan, J.M., Krause, D.S., Lee, A.I., Halene, S., et al. (2021). Thrombocytopeny and endotheliopathy: crucial contributors to COVID-19 thromboinflammation. *Nat. Rev. Cardiol.* *18*, 194–209. <https://doi.org/10.1038/s41569-020-00469-1>.
51. Bonaventura, A., Vecchié, A., Dagna, L., Martinod, K., Dixon, D.L., Van Tassel, B.W., Dentali, F., Montecucco, F., Massberg, S., Levi, M., et al. (2021). Endothelial dysfunction and immunothrombosis as key pathogenic mechanisms in COVID-19. *Nat. Rev. Immunol.* *21*, 319–329. <https://doi.org/10.1038/s41577-021-00536-9>.
52. Faraday, N., Schunke, K., Saleem, S., Fu, J., Wang, B., Zhang, J., Morrell, C., and Dore, S. (2013). Cathepsin G-dependent modulation of platelet thrombus formation in vivo by blood neutrophils. *PLoS One* *8*, e71447. <https://doi.org/10.1371/journal.pone.0071447>.
53. Ni, H., Yuen, P.S.T., Papalia, J.M., Trevithick, J.E., Sakai, T., Fässler, R., Hynes, R.O., and Wagner, D.D. (2003). Plasma fibronectin promotes thrombus growth and stability in injured arterioles. *Proc. Natl. Acad. Sci. USA* *100*, 2415–2419. <https://doi.org/10.1073/pnas.2628067100>.
54. Frantz, S., Hofmann, U., Fraccarollo, D., Schäfer, A., Kranepuhl, S., Hagedorn, I., Nieswandt, B., Nahrendorf, M., Wagner, H., Bayer, B., et al. (2013). Monocytes/macrophages prevent healing defects and left ventricular thrombus formation after myocardial infarction. *FASEB J.* *27*, 871–881. <https://doi.org/10.1096/fj.12-214049>.
55. Thomas, G., Tacke, R., Hedrick, C.C., and Hanna, R.N. (2015). Nonclassical patrolling monocyte function in the vasculature. *Arterioscler. Thromb. Vasc. Biol.* *35*, 1306–1316. <https://doi.org/10.1161/ATVBAHA.114.304650>.
56. Zhu, Y., Chen, X., and Liu, X. (2022). NETosis and Neutrophil Extracellular Traps in COVID-19: Immunothrombosis and Beyond. *Front. Immunol.* *13*, 838011. <https://doi.org/10.3389/fimmu.2022.838011>.
57. Massena, S., Christoffersson, G., Vågesjö, E., Seignez, C., Gustafsson, K., Binet, F., Herrera Hidalgo, C., Giraud, A., Lomei, J., Weström, S., et al. (2015). Identification and characterization of VEGF-A-responsive neutrophils expressing CD49d, VEGFR1, and CXCR4 in mice and humans. *Blood* *126*, 2016–2026. <https://doi.org/10.1182/blood-2015-03-631572>.
58. Evans, C.E., Humphries, J., Mattock, K., Saha, P., and Smith, A. (2012). HIF1 signalling regulates venous thrombus resolution. *Thromb. Res.* *130*, 971–973. <https://doi.org/10.1016/j.thromres.2012.08.002>.
59. Evans, C.E., Humphries, J., Mattock, K., Waltham, M., Wadoodi, A., Saha, P., Modarai, B., Maxwell, P.H., and Smith, A. (2010). Hypoxia and upregulation of hypoxia-inducible factor 1{alpha} stimulate venous thrombus recanalization. *Arterioscler. Thromb. Vasc. Biol.* *30*, 2443–2451. <https://doi.org/10.1161/ATVBAHA.110.215038>.
60. Varma, M.R., Varga, A.J., Knipp, B.S., Sukheepod, P., Upchurch, G.R., Kunkel, S.L., Wakefield, T.W., and Henke, P.K. (2003). Neutropenia impairs venous thrombosis resolution in the rat. *J. Vasc. Surg.* *38*, 1090–1098. [https://doi.org/10.1016/S0741-5214\(03\)00431-2](https://doi.org/10.1016/S0741-5214(03)00431-2).
61. Wardlaw, J.M., Murray, V., Berge, E., and Del Zoppo, G.J. (2009). Thrombolysis for acute ischaemic stroke. *Cochrane Database Syst. Rev.* *2014*, CD000213. <https://doi.org/10.1002/14651858.CD000213.pub2>.
62. Wardlaw, J.M., Murray, V., Berge, E., and del Zoppo, G.J. (2014). Thrombolysis for acute ischaemic stroke. *Cochrane Database Syst. Rev.* *2016*, CD000213. <https://doi.org/10.1002/14651858.CD000213.pub3>.
63. Emberson, J., Lees, K.R., Lyden, P., Blackwell, L., Albers, G., Bluhmki, E., Brott, T., Cohen, G., Davis, S., Donnan, G., et al. (2014). Effect of treatment delay, age, and stroke severity on the effects of intravenous thrombolysis with alteplase for acute ischaemic stroke: a meta-analysis of individual patient data from randomised trials. *Lancet* *384*, 1929–1935. [https://doi.org/10.1016/S0140-6736\(14\)60584-5](https://doi.org/10.1016/S0140-6736(14)60584-5).
64. Kerber, E.L., Padberg, C., Koll, N., Schuetzhold, V., Fandrey, J., and Winning, S. (2020). The Importance of Hypoxia-Inducible Factors (HIF-1 and HIF-2) for the Pathophysiology of Inflammatory Bowel Disease. *Int. J. Mol. Sci.* *21*, 8551. <https://doi.org/10.3390/ijms21228551>.
65. Parekh, S., Ziegenhain, C., Vieth, B., Enard, W., and Hellmann, I. (2018). zUMIs - A fast and flexible pipeline to process RNA sequencing data with UMIs. *Gigascience* *7*, giy059. <https://doi.org/10.1093/gigascience/giy059>.
66. Mathew, D., Giles, J.R., Baxter, A.E., Oldridge, D.A., Greenplate, A.R., Wu, J.E., Alanio, C., Kuri-Cervantes, L., Pampena, M.B., D’Andrea, K., et al. (2020). Deep immune profiling of COVID-19 patients reveals distinct immunotypes with therapeutic implications. *Science* *369*, eabc8511. <https://doi.org/10.1126/science.abc8511>.

67. Van Gassen, S., Callebaut, B., Van Helden, M.J., Lambrecht, B.N., Demeester, P., Dhaene, T., and Saeys, Y. (2015). FlowSOM: Using self-organizing maps for visualization and interpretation of cytometry data. *Cytometry A* 87, 636–645. <https://doi.org/10.1002/cyto.a.22625>.
68. Huang da, W., Sherman, B.T., and Lempicki, R.A. (2009). Bioinformatics enrichment tools: paths toward the comprehensive functional analysis of large gene lists. *Nucleic Acids Res.* 37, 1–13. <https://doi.org/10.1093/nar/gkn923>.
69. Huang da, W., Sherman, B.T., and Lempicki, R.A. (2009). Systematic and integrative analysis of large gene lists using DAVID bioinformatics resources. *Nat. Protoc.* 4, 44–57. <https://doi.org/10.1038/nprot.2008.211>.
70. Hao, Y., Hao, S., Andersen-Nissen, E., Mauck, W.M., III, Zheng, S., Butler, A., Lee, M.J., Wilk, A.J., Darby, C., Zager, M., et al. (2021). Integrated analysis of multimodal single-cell data. *Cell* 184, 3573–3587.e29. <https://doi.org/10.1016/j.cell.2021.04.048>.
71. Smedley, D., Haider, S., Ballester, B., Holland, R., London, D., Thorisson, G., and Kasprzyk, A. (2009). BioMart – biological queries made easy. *BMC Genomics* 10, 22. <https://doi.org/10.1186/1471-2164-10-22>.
72. Gu, Z., Eils, R., and Schlesner, M. (2016). Complex heatmaps reveal patterns and correlations in multidimensional genomic data. *Bioinformatics* 32, 2847–2849. <https://doi.org/10.1093/bioinformatics/btw313>.
73. Bhusal, R.P., Eaton, J.R.O., Chowdhury, S.T., Power, C.A., Proudfoot, A.E.I., Stone, M.J., and Bhattacharya, S. (2020). Evasins: Tick Salivary Proteins that Inhibit Mammalian Chemokines. *Trends Biochem. Sci.* 45, 108–122. <https://doi.org/10.1016/j.tibs.2019.10.003>.
74. Armingol, E., Officer, A., Harismendy, O., and Lewis, N.E. (2021). Deciphering cell–cell interactions and communication from gene expression. *Nat. Rev. Genet.* 22, 71–88. <https://doi.org/10.1038/s41576-020-00292-x>.
75. La Manno, G., Soldatov, R., Zeisel, A., Braun, E., Hochgerner, H., Petukhov, V., Lidschreiber, K., Kastrioti, M.E., Lönnerberg, P., Furlan, A., et al. (2018). RNA velocity of single cells. *Nature* 560, 494–498. <https://doi.org/10.1038/s41586-018-0414-6>.
76. Whiting, D., and DiNardo, J.A. (2014). TEG and ROTEM: technology and clinical applications. *Am. J. Hematol.* 89, 228–232. <https://doi.org/10.1002/ajh.23599>.

STAR★METHODS

KEY RESOURCES TABLE

REAGENT or RESOURCE	SOURCE	IDENTIFIER
Antibodies		
Rat Anti mouse Ly6G-FITC	Biolegend	127606
Rat Anti mouse Ly6G-PE	Biolegend	127608
TotalSeq B hashtag #7	Biolegend	394643
TotalSeq B hashtag #8	Biolegend	394645
TotalSeq B hashtag #9	Biolegend	394647
CITE-Seq anti-human CD41	Biolegend	303747
CITE-Seq anti-human CD16	Biolegend	302063
CITE-Seq anti-human CD10	Biolegend	312235
CITE-Seq anti-human CD14	Biolegend	367145
CITE-Seq anti-human CD15	Biolegend	323051
Mouse anti-human CD16-APC	Biolegend	302012
Mouse anti-human CD14-FITC	Biolegend	301803
Mouse anti-human CD45-APC/Cyanine7	Biolegend	368515
Mouse anti-human CD16 PE-Cy7	Biolegend	302015
Mouse anti-human CD15 APC	Biolegend	301907
Mouse anti-human CD45 FITC	Biolegend	982316
Mouse anti-human CD15-PE/Cyanine7	Biolegend	323030
Mouse anti-human CD16-APC	Biolegend	302012
Goat anti-human/mouse MPO	R&D Systems	AF3667
Purified rat anti-mouse Ly6G	Biolegend	127601
Rabbit anti-human MPO	DAKO	GA51161-2
Goat anti-human/mouse MPO	R&D Systems	AF3667
Rabbit anti-human/mouse/rat PLAUR	Bioss	Bs-1927R
Rabbit anti-human Urokinase	Abcam	Ab24121
Rabbit anti-human CD3	Zytomed Systems GmbH	RBK024
Mouse anti-human CD4	Leica Biosystems	CD4-368-L-CE
Mouse anti-human CD8	Cell Marque Tissue Diagnostics	108M-98
Rabbit anti-human CD14	Zytomed Systems	RBK033-05
Mouse anti-human CD15	Abcam	ab233867
Mouse anti-human CD20	Dako	M0755
Anti-human CD45-BV650	Biolegend	304044
Anti-human CD14-FITC	BD Pharmigen	557153
Anti-human Siglec 8-Percp-Cy5.5	Biolegend	347107
Anti-human CD15-APC	Biolegend	301908
Anti-human CD19-APC-Cy7	Biolegend	363010
Anti-human HLA-DR-BV605	Biolegend	307640
Anti-human CD123-BV785	Biolegend	306032
Anti-human CD3-BV510	Biolegend	317332
Anti-human CD56-BV711	Biolegend	362542
Anti-human CD34-A.F.700	Biolegend	343622
Anti-human CD41-Pacific Blue	Biolegend	303714
Anti-human CD63-BV650	Biolegend	353026
Anti-human CD177-FITC	Biolegend	315804
Anti-human VEGFR1	MACS Miltenyi Biotec	130-124-438

(Continued on next page)

Continued

REAGENT or RESOURCE	SOURCE	IDENTIFIER
Anti-human TCR α/β -Percp-Cy5.5	Biologend	306724
Anti-human CD184-APC-Cy7	Biologend	306528
Anti-human CD49d-BV605	Biologend	304324
Anti-human CD62L-BV785	Biologend	304830
Anti-human CD16-BV510	Biologend	302048
Anti-human VD11b-BV711	Biologend	301344
Anti-human IL-17A-A.F.700	Biologend	512318
Anti-human CD31-PE-Dazzle	Biologend	303130
Anti-human CD284-PE-Cy7	Invitrogen	25-9917-42
Anti-human CD93-PE	Biologend	336108
Anti-human CD36-Percp-Cy5.5	Biologend	336224
Anti-human SLAN-APC	MACS Miltenyi Biotec	130-117-919
Anti-human IgE-APC-Fire750	Biologend	325516
Anti-human HLA-DR-BV605	Biologend	307640
Anti-human CD192-BV786	Biologend	357234
Anti-human CD86-BV711	Biologend	305440
Anti-human CD11c-A.F.700	Biologend	337220
Anti-human CD11a-PE-Dazzle	Biologend	301232
Anti-human CD9-PE-Cy7	Biologend	312116
Anti-human CD45-FITC	Biologend	368508
Anti-human CD14-FITC	BD Biosciences	558121
Anti-human CD16-PE-Cy7	BD Biosciences	557744
Anti-human Siglec8-Percp-Cy5.5	Biologend	347107
Anti-human CD19-APC-Cy7	Biologend	363010
Anti-human CD3-BV510	Biologend	317332
Anti-human CD56-APC-Cy7	Biologend	362512
Anti-human CD3-PE	Biologend	300308
Anti-human CD20-PE	Biologend	302306
Chemicals, peptides, and recombinant proteins		
Sybr green (SsoAdvanced Universal SYBR Green Supermix)	Biorad	172-5272
Roxadustat	Selleckchem	S1007
RPMI medium	Bio&SELL GmbH	BS.F1415
FBS	Bio&SELL GmbH	FBS.S.0615
Glutamine	Gibco	2146978
Thrombin	Sigma-Aldrich	T7326-1KU
Dulbecco's Phosphate Buffered Saline	Sigma-Aldrich	D8537
BD Pharm Lyse Lysing Buffer	BD Biosciences	555899
RLT Plus Buffer	Qiagen	1053393
Proteinase K	Life Technologies	AM2548
Cleanup Beads	GE65152105050250	Sigma-Aldrich
DNase I	Thermo Fisher	EN0521
Maxima H- enzyme	Thermo Fisher	EP0753
Maxima H- Buffer	Thermo Fisher	EP0753
dNTPs	Thermo Fisher	R0186
Exonuclease I	New England Biolabs	M0293L
KAPA HS Ready Mix	Roche	07958935001
DNase/RNase-Free Distilled Water	ThermoFisher	10977-049
Q5 Master Mix	New England Biolabs	M0544L

(Continued on next page)

<i>Continued</i>		
REAGENT or RESOURCE	SOURCE	IDENTIFIER
SPRI-select Beads	Beckman Coulter	B23317
human serum albumin	Sigma-Aldrich	A9731-5G
human fibrinogen conjugated with AF488	Invitrogen	F13191
Hoechst 33342	Invitrogen	H3570
SYTOX™ Orange dead cell stain	ThermoFisher	S34861
Albumin Fraction V	Carl Roth GmbH & Co. KG	8076.4
EDTA	AppliChem GmbH	A4892
Sytox Blue live/dead dye	Invitrogen	S34857
Fluorescent Mounting Medium	DAKO	S3023
Sytox red live/dead dye	DAKO	S34859
CellTracker™ Red CMTPX Dye	ThermoFisher	C34552
Reparixin	Selleckchem	S8640
DAPI	Merck	10236276001
StarTEG solution	Tem Innovations GmbH	503-10
EXTEM solution	Tem Innovations GmbH	503-05
<i>Critical commercial assays</i>		
EasySep™ Direct Human Neutrophil Isolation Kit	Stemcell™ Technologies	19666
High Capacity cDNA Reverse Transcription Kit	Applied Biosystems	4368814
Quant-iT PicoGreen dsDNA Assay Kit	ThermoFisher	P7581
High-Sensitivity DNA Kit	Agilent	5067-4627
NEBNext Ultra II FS Library Preparation Kit	New England Biolabs	E6177S
Single Cell 3' reagent kit v3.1	10X Genomics	CG000206 RevD
UltraView Universal DAB Detection Kit	Roche	05269806001
<i>Deposited data</i>		
Sequencing data are available at	Zenodo	https://doi.org/10.5281/zenodo.10466853
<i>Experimental models: Organisms/strains</i>		
Mouse: C57BL/6	The Jackson Laboratory	000664
Nur77 ^{-/-}	The Jackson Laboratory	006187
Lyz2-cre;Hif1a ^{fl/fl}	Kerber et al. ⁶⁴	Sandra Winning and Joachim Fandrey (originally via the JAX laboratory)
<i>Oligonucleotides</i>		
human Beta-Actin	Qiagen	QT01680476
Human Plau	Qiagen	QT00013426
Human Vegfa	Qiagen	QT01010184
Human Vegfb	Qiagen	QT00013783
<i>Software and algorithms</i>		
FlowJo	BD Bioscience	V. 10.10.0
FlowJo	BD Bioscience	10.8.14
Fastqc		version 0.11.8
Cutadapt		version 1.12
zUMIs pipeline	Parekh et al. ⁶⁵	version 2.9.4d
Gencode annotation (v35) using STAR		version 2.7.3a
RSubread		version 1.32.4
DESeq2		version 1.30.0
CellRanger	10X Genomics	v6.0.1 and v6.1.1
R		version 4
Seurat		v4.0.4

(Continued on next page)

Continued

REAGENT or RESOURCE	SOURCE	IDENTIFIER
Seurat		v4.1.1
CellRanger	10X Genomics	v6.1.1
Monocle3	cole-trapnell-lab/monocle3	March 2023
QuPath platform		v0.50
Prism	Graphpad	V10.4.1
Other		
FALCON	Corning	352350
BD Vacutainer CPT tubes	BD Biosciences	362780
ibiTreat μ -Slides	Ibidi GmbH	80606
Reagent Cups (ROTEM)	Tem Innovations GmbH	200011
Citrate tubes	SARSTEDT AG & Co. KG	04.1952.100

EXPERIMENTAL MODEL AND STUDY PARTICIPANT DETAILS

Ethics and patient cohort

In accordance with the Declaration of Helsinki and with the approval of the Ethics Committee of Ludwig-Maximilian-University Munich (No: 121-09 and 20-0809) and Ethics Committee of the Technical University of Munich (No.: 635/21 S-NP, 5518/12) informed consent of the patients or their guardians was obtained for the multi-omic analyses, retrospectively analysed samples were anonymized. There was no participant compensation. Samples from a total of 32 patients with acute stroke were included into the study for multi-omic analyses. After thrombectomy, thrombi were rinsed with saline to wash away possible non-thrombus cells. Blood was collected by phlebotomy within 90 minutes after thrombectomy in EDTA (for flow cytometry and FACS-sort) or heparin-buffered tubes (for scRNA-seq).

Deep vein thrombosis - Mouse model of flow restriction in the IVC

All animal studies were approved by the local legislation on protection of animals (Regierung von Oberbayern, Munich (55.2-2532.Vet_02-20-190, 55.2-2532.Vet_02-16-138)). The mouse model of flow restriction in the IVC was performed as described before.⁴ For anesthesia and pain-treatment Fentanyl, Midazolam, Medetomidin with subsequent Buprenorphin were used. After a median laparotomy the IVC was exposed and a space holder was positioned followed by a narrowing ligature. Subsequently, the wire was removed to avoid complete vessel occlusion. Side branches were not ligated or manipulated. All groups were age, sex, and weight matched. Mice were between 12 and 25 weeks of age at the time of inclusion into experiments, all mice were on C57/B6 background and bone-marrow recipient mice were C57/B6 mice. Mice with bleedings or any injury of the IVC during surgery were excluded from further analysis. For thrombus weight measurement after 48 hours, the IVC was excised just below the renal veins and proximal to the confluence of the common iliac veins. *Nr4a1*^{-/-} mice were bought from Jackson Laboratories. *Lyz2-cre*; *Hif1 α* ^{fl/fl} mice and *Hif1 α* ^{fl/fl} control mice were kindly provided by S.W. and J.F.

Intravital neutrophil fate mapping

All animal studies were approved by the local legislation on protection of animals (Regierung von Oberbayern, Munich (55.2-2532.Vet_02-20-190, 55.2-2532.Vet_02-16-138)). Directly before the flow restriction of the IVC, FITC anti-mouse Ly-6G antibody was injected i.v. into the mouse tail vein (5 μ g/25g mouse, Clone 1A8, Biolegend). 48 hours after the first FITC anti-mouse Ly-6G antibody injection, PE anti-mouse Ly-6G Antibody was injected i.v. into the tail vein of the same mice (5 μ g/25g mouse, Clone 1A8, Biolegend). 24 hours after the second injection (72 hours after the restriction of the IVC), the IVC was collected, embedded in OCT and stored at -80°C for histology.

Bone marrow transplant

All animal studies were approved by the local legislation on protection of animals (Regierung von Oberbayern, Munich (55.2-2532.Vet_02-20-190, 55.2-2532.Vet_02-16-138)). Bone marrow chimeras were generated by irradiation of recipient C57Bl6 mice. Six- to eight-week-old mice were irradiated twice within a 4-h interval (195 kV, 10 mA) and received isolated bone marrow from control C57/Bl6 mice or *Nr4a1*^{-/-} mice on C57/Bl6 background (The Jackson Laboratory, Cat.: 006187). Bone-marrow from *Lyz2-cre*; *Hif1 α* ^{fl/fl} mice (referred to as *Lyz2-cre*; *Hif1 α* ^{fl/fl} mice) was generously provided by Sandra Winning and Joachim Fandrey and was transplanted accordingly into C57/Bl6 mice.

METHOD DETAILS

Single-cell preparation and flow-cytometry

Thrombi immediately after harvesting were brought into single-cell suspension by gently pushing across a 70 μ m Cell Strainer (FALCON, Cat# 352350) into PBS (Sigma-Aldrich, Cat# D8537) and subsequently centrifuged (350rcf, 4°C, 7 minutes). For flow-cytometry based phenotyping and single-cell RNA Seq approaches, the pellet was resuspended in FACS Buffer (PBS with 0,5% BSA). The thrombus cell suspension and the patient's blood were each mixed with the same amount of antibody mix (see [antibody](#) below) and incubated. Erythrocyte depletion was performed by incubation with 500 μ l of BD Pharm Lyse Lysing Buffer (BD Biosciences, Cat# 555899), blood and thrombi were processed alike. For the flow-cytometry based monocyte and the neutrophil phenotyping, the thrombus cell-pellet as well as 200 μ l of the patient's blood was each mixed with 6ml of RBC lysis buffer (containing 20g NH₄Cl (1,5M), 2,5g KHCO₃ (0,1M), 5ml 0,5M EDTA (10mM) and 250ml distilled water) for 10 minutes. The lysing process was stopped by addition of 6ml of cold PBS and repeated with blood after centrifugation, then samples were centrifuged and resuspended in FACS Buffer and incubated 1:1 with the respective antibody mix. For downstream 10X single-cell sequencing assays, BD Lysing buffer (Cat.: 555899) was used instead of the above-mentioned procedure for erylisis. After another centrifugation step, both samples were resuspended in FACS Buffer.

The dead cell stain was added before flow-cytometry. Flow cytometry was always performed with a LSRFortessa Flow Cytometer (BD Biosciences).

Flow-cytometry analysis was performed using FlowJo (BD). Thrombi containing mainly cell debris were not included into further analysis. For cluster identification, FlowSOM was used as described previously,^{46,66,67} visualization was done using t-SNE.

RT-PCR of isolated neutrophils from young versus older thrombi

Thrombus formation in healthy blood was induced by addition of CaCl₂ (1 mM) and Thrombin (1 U/ml). Thrombi and corresponding blood were incubated at 37°C and 5% CO₂. Thrombi were put through a 70 μ m cell strainer for single cell suspension. After centrifugation (4°C, 350g, 7 min) the pellets were resuspended in PBS with 1 mM EDTA. Neutrophil isolation was performed according to manufacturer's instructions (StemcellTM Technologies EasySepTM Direct Human Neutrophil Isolation Kit Catalog #19666). Pellets were resuspended in RLT Buffer and qPCR was performed using Sybr green (SsoAdvanced Universal SYBR Green Supermix #172-5272, Biorad), High Capacity cDNA Reverse Transcription Kit (#4368814, Applied Biosystems), and the following primers from Qiagen: QT01680476 (human Beta-Actin), QT00013426 (human PLAU), QT01010184 (human VEGFA), QT00013783 (human VEGFB).

Thrombus clearance by Roxadustat-stimulated neutrophils

Human neutrophils were freshly isolated by EasySep Direct Human Neutrophil Isolation Kit (STEMCELL Technologies, #19666) and incubated with 50 μ M Roxadustat for 36 hours as 1 million cells/ml in RPMI medium (RPMI medium (Bio&SELL GmbH, #BS.F1415) containing 10% FBS (Bio&SELL GmbH, #FBS.S.0615), and 2 mM glutamine (Gibco, #2146978)). The neutrophils were harvested by centrifugation at 320rcf, at room temperature for 7 minutes, and the pellets were resuspended in RPMI containing 20% human plasma and 2 mM glutamine. Cell counts were determined using a Bio-Rad TC20 automated cell counter, and cell density was normalized to 1 million cells/ml in RPMI containing human plasma. Fresh neutrophils were isolated from the same corresponding healthy donors and similarly normalized to 1 million cells/ml with RPMI containing human plasma. Artificial thrombi were generated from 1ml of fresh blood of health donors by adding 1 mM CaCl₂ and 1 U/ml thrombin (Sigma-Aldrich, #T7326-1KU) as final concentrations to citrate anticoagulated blood. After incubation at room temperature for 1 hour to allow thrombus formation, the thrombi were removed, individually weighed, and transferred into 6-well plates. Each thrombus was then mixed with 1 million cells/ml of stimulated or fresh neutrophils in RPMI containing 10% human plasma. Incubation performed at 37°C with 5% CO₂, and thrombus weight was measured every 2 hours.

scRNA-seq of real and artificial (*in vitro* generated) thrombus

Patient thrombus and blood (citrate blood collection tube) were collected and immediately processed as follows: 3ml of patient blood was transferred to a 15ml facon tube for artificial thrombus generation through the addition of CaCl₂ and thrombin as previously described. The sample was rapidly mixed and incubated for 3 hours at 37°C and 5% CO₂. After 3 hours, the artificial thrombus was pressed through a 70 μ m filter into a 50ml falcon tube with flow-cytometry buffer and centrifuged (300g, 5mins at 4°C). The pellet was resuspended in BD Pharm LyseTM lysing buffer with a wide-bore pipette and incubated for 13 minutes on ice. Following erylisis, the cell suspension was centrifuged (300g, 5 mins at 4°C) and resuspended in Fc-block and incubated on ice for 10 minutes. The remainder of the patient blood was erylised with BD Pharm LyseTM lysing buffer for 13 minutes at RT. The erylised blood was centrifuged (300g, 5mins at 4°C) after which the pellet was resuspended in Fc-block and incubated for 10 minutes on ice. The real thrombus was processed in the same manner as the artificial thrombus which was outlined previously. Following Fc-block incubation, the cells from the blood, artificial and real thrombus were incubated in anti-human TotalSeq B hashtag (#7 (Biolegend, #394643), #8 (Biolegend, #394645) and #9 (Biolegend, #394647) respectively) and CITE-seq (CD41 (Biolegend, #303747) and CD16 (Biolegend, #302063)) antibody mastermix for 30 minutes on ice. The cells were then washed with 5ml flow-cytometry buffer and centrifuged (250g, 10 mins at 4°C). The resulting supernatant was resuspended in 5ml flow-cytometry buffer and passed through a 50 μ m filter. The filtrate was then washed twice (250g, 10mins at 4°C) and resuspended in 20 μ l PBS with 0.04% BSA and counted with diluted

trypan blue. The three samples were adjusted to a concentration of 1000 cells/ μ l and pooled together. Approximately 60,000 cells from the pooled samples were loaded into the chromium controller for single cell library generation.

Preparation for prime-seq RNAseq of blood and thrombus neutrophils and monocytes

This was performed as published before.²⁰ Whole blood and the thrombus single-cell suspension were treated following the same erythrocyte lysis protocol as previously described for the monocyte and neutrophil FACS preparation and then stained with the respective antibody mix. After 20 minutes of incubation, the samples were washed and dead cell stain was added directly before isolating the different cell populations by FACS Sort (using the MoFlo Astrios EQ, Beckman Coulter). The isolated monocytes or neutrophils were sorted into RLT Plus Buffer with 1% β -mercaptoethanol in low-binding RNA tubes. RNA from approximately 400 sorted CD15⁺ neutrophils and 200 CD14⁺ sorted monocytes were included for the subsequent prime-RNA sequencing (prime-Seq²⁰).

prime-seq

prime-seq is a sensitive and efficient early barcoding bulk RNA-seq method described in detail in Janjic et al.²⁰ and at protocols.io (<https://doi.org/10.17504/protocols.io.s9veh66>). In summary, the RLT Plus Buffer (Qiagen®) with 1% β mercapto-ethanol and the included cells were further processed for library preparation. Lysate treatment was performed with Proteinase K (AM2548, Life Technologies®), isolation was performed with cleanup beads (GE65152105050250, Sigma-Aldrich®) (2:1 beads/sample ratio), and genomic DNA digestion was performed with DNase I (EN0521, Thermo Fisher®). Reverse transcription was performed with 30 units of Maxima H- enzyme (EP0753, Thermo Fisher®), and 1x Maxima H- Buffer (EP0753, Thermo Fisher®), 1 mM each dNTPs (R0186, Thermo Fisher®), 1 μ M template-switching oligo (IDT), 1 μ M barcoded oligo-dT primers (IDT) in a 10 μ L reaction volume at 42 °C for 90 minutes. Samples from the same cell type were then pooled and cleaned using cleanup beads (1:1 beads/sample ratio). Exonuclease I (M0293L, NEB) was used to digest remaining primers following cleanup at 37 °C for 20 minutes followed by 80 °C for 10 minutes. Subsequently, the digested samples were again cleaned using cleanup beads (1:1 beads/sample ratio).

Synthesis of second strand and pre-amplification was subsequently performed using 1X KAPA HS Ready Mix (07958935001, Roche®) and 0.6 μ M SINGV6 primer (IDT) in a 50 μ L reaction. PCR cycles were set as follows: 98 °C for 3 minutes; 15 cycles of 98 °C for 15 s, 65 °C for 30 s, 72 °C for 4 minutes; and 72 °C for 10 minutes. Next, cleanup beads were used (0.8:1 beads/sample ratio) and then eluted in 10 μ L of DNase/RNase-Free Distilled Water (10977-049, ThermoFisher®). cDNA was quantified by the Quant-iT PicoGreen dsDNA Assay Kit (P7581, Thermo Fisher®), the distribution of size was qualified by the High-Sensitivity DNA Kit (5067-4627, Agilent®). Pre-sequencing QC was performed by Bioanalyzer traces. A total of 400 and 200 cells were included for neutrophils and for monocytes. Viability was checked during FACS-sorting, as dead cells were excluded by respective gating. The only phred based filtering in prime-seq was performed in the UMI and BC, where we had a cut off for 4 BC bases and 5 UMI bases, with a phred lower than 20. We did this to remove any data from the start that might have low sequencing quality and therefore could cause issues with demultiplexing based on the barcodes. Since the barcodes are 12 bases long, a cutoff of 4 is sufficient as anything lower would still allow a proper demultiplexing. We did not perform any filtering based on phred score of the cDNA read as part of pre-processing. Mapping Quality controls were done using the default parameters in STAR.

After quality control, cDNA was used to make libraries with the NEBNext Ultra II FS Library Preparation Kit (E6177S, NEB), using a five-fold lower reaction volume than instructed by the manufacturer. The Enzyme Mix supplied and Reaction buffer was used for fragmentation in a 6 μ L reaction. Adapter ligation was performed by the supplied Ligation Enhancer, Ligation Master Mix, and an additional custom prime-seq Adapter (1.5 μ M, IDT) in a reaction volume of 12.7 μ L. Following ligation, double-size selection using SPRI-select Beads (B23317, Beckman Coulter®), with 0.5 and 0.7 ratios, was performed. Subsequently, sample amplification was performed using a library PCR using Q5 Master Mix (M0544L, NEB), 1 μ L i7 Index primer (Sigma-Aldrich®), and 1 μ L i5 Index primer (IDT) using the following setup: 98 °C for 30 s; 13 cycles of 98 °C for 10 s, 65 °C for 1 m 15 s, 65 °C for 5 m; and 65 °C for 4 m. Final double size selection was performed using SPRI-select Beads.

Concentration and quality were analysed using a high-sensitivity DNA chip (Agilent Bioanalyzer), subsequently the libraries were 150 bp paired-end sequenced on a NextSeq (Illumina®).

ScRNA-seq of human and mouse blood and thrombi

The Chromium Next GEM Single Cell 3' reagent kit v3.1 (CG000206 Rev D) from 10X Genomics® protocol was used for library preparation. To decrease batch-effect related artifacts, sample multiplexing with TotalSeqB™ anti-human or anti-mouse hashtag antibodies, was performed. According to the manufacturer's instructions, first GEMs (Gel bead-in-Emulsion) were generated, reverse transcription was performed subsequently, and cDNA was cleaned up, amplified, and size selected subsequently. After quantification and QC, gene expression libraries and cell surface libraries were constructed. The libraries were then sequenced with an Illumina NovaSeq.

CITE-Seq

The method of Cellular Indexing of Transcriptomes and Epitopes by sequencing (CITE-Seq) has allowed us to combine the analysis of surface markers and gene expression for cell phenotyping. We used the following antibodies from BioLegend: CD10 (HI10a, Cat# 312235), CD14 (clone 63D3, Cat# 367145), CD15 (clone W6D3, Cat# 323051) and CD16 (clone 3G8, Cat# 302063). Anti-CD16

antibody was employed to n=3-4 blood and thrombi, Anti CD10, CD14 and CD15 was employed to n=3 blood and thrombi, respectively. This excludes the comparison between blood, real thrombus and artificial thrombus where the Anti-CD16 and Anti-CD41 antibody were included (as further described above).

Bioinformatic analysis of prime-seq data

Fastqc was used to initially check the data (version 0.11.8). Cutadapt (version 1.12) was used to remove any regions on the 3' end of the read where the sequence read into the poly-A tail. To filter the data, the zUMIs pipeline (version 2.9.4d, Parekh et al., 2018) was used, using a phred threshold of 20 for 4 bases for both the UMI and BC, to map the reads to the human genome with the Gencode annotation (v35) using STAR (version 2.7.3a), and count the reads using RSubread (version 1.32.4).

Differential Gene Expression Analysis

Differential gene expression analysis on the bulk RNA-Seq data was performed using the poreSTAT differential expression analysis pipeline (<https://github.com/mjoppich/poreSTAT/>, work in progress). Differential gene expression results used in this manuscript were obtained from calling DESeq2 (version 1.30.0) with default parameters on the read counts from the zUMIs pipeline (see above). On the neutrophil bulk RNA-seq dataset 2 thrombi and 1 blood samples were removed due to too low read counts. Samples failed: 3 out of 34. Low read counts were defined as less than 140,000 reads.

Overrepresentation analysis

Overrepresentation analysis on the prime-seq²⁰ data was performed using the DAVID web interface.^{68,69}

scRNAseq data analysis

Data were obtained and processed using Cell Ranger (v6.0.1 and v6.1.1) using the mm10-2020-A (for mouse data) and the GRCh38-2020-A (for human data) reference genomes. Cell Ranger was run using default parameters and with custom feature references. The 21053 runs were run with both antibody capture references Htag9 and Htag10 for differentiating blood and thrombus samples. The mouse data was run with antibody capture references for mouse antibodies 1-10. Finally, the remaining human samples were run with antibody capture references Htag1-Htag10 and CD10, CD14, CD15 and/or CD16.

The subsequent analysis was performed in R version 4 with Seurat⁷⁰ v4.0.4 (mouse) and v4.1.1 (human). For the mouse dataset, the raw counts were used and filtered such that cells have between 100 and 6,000 features and at least 200 UMIs. Cells were removed if more than 15% of the UMIs per cell were of mitochondrial origin. The dataset was split according to the hashtag identified by following the HTO (Hash Tag Oligo) demultiplexing vignette of Seurat. For each library, HTO demultiplexing was performed according to the Seurat vignette with `positive.quantile=0.99`. Results were additionally checked using ridge plots on the HTO expression. Only cells with global identification as singlets were kept (negative and doublet cells were removed). Each sample was normalized using Seurat's `NormalizeData` function and variable features were determined as per the standard Seurat analysis pipeline. Human cell-cycle genes from Seurat were converted to mouse using the `biomart`⁷¹ library. The samples were scaled, regressing out `percent.rp`, `percent.mt`, `nCount_RNA` as well as `S.Score` and `G2m.Score` from Seurat's `CellCycleScoring` function. A total of 61,943 cells were included for subsequent analyses. The samples were then integrated using `rPCA` with 3000 anchor features and 50 PCs. The integrated object was scaled, and PCA was run. UMAP and neighbors were identified from the first 50 PCs. Clusters were identified at a resolution of 0.2. Differential gene expression was calculated using the t-test implemented in Seurat.

The human datasets were loaded into Seurat objects in a library-wise pattern from the raw Cell Ranger output. The samples were filtered such that cells have at least 100 UMIs and between 100 and 6,000 features in order to capture also neutrophils, which have little RNA expression. For each library, HTO demultiplexing was performed according to the Seurat vignette. After HTO demultiplexing, the libraries were each normalized and variable features were detected. A total of 4,000 integration features was selected for scaling the libraries regressing out `percent.rp`, `percent.mt`, `nCount_RNA` as well as `S.Score` and `G2m.Score` from Seurat's `CellCycleScoring` function, which was also run on the libraries. Integration itself was performed for all libraries using 3,000 integration features and following the reciprocal PCA integration vignette using 30 PCs and 10 anchors for integration. After integration, the antibody capture for the CITE-seq counts was prepared. For each library, the counts were subset such that the normalization using the CLR method with margin 2 was performed on only those antibodies that were measured in the respective samples. According to the recommendations of the Seurat authors, CLR normalization was conducted with margin 2, because both the hashtag oligonucleotides as well as the CITE-seq antibodies are competing in binding to the GEM, and thus CITE-seq antibodies could not be guaranteed to attach to saturation (which would be the assumption using margin 1 normalization). In order to add the assay to the integrated object, the count matrix was extended with zeros for all remaining cells for all antibodies. There is no further integration of the CITE-seq counts required, because CITE-seq counts were not used for integrating the samples, nor for dimensionality reduction. In analogy to the RNA assay, any expression analysis is performed on the unscaled per-cell-normalized ADT values. Heatmaps were created using the `ComplexHeatmap` package on the `scale.data` slot of the RNA assay of the scRNA-seq data.⁷²

We performed condition-wise gene module detection using the method and script provided by Kazer et al.⁴⁵ In brief, this method takes the gene expression values of the genes represented by the first few principal components of the scRNA-seq object as input for WGCNA functions. Here, we chose the maximal 500 genes reported by the `PCASigGenes` function of Seurat for each of the first eight PCs. The resulting adjacency matrix is transformed into a topological overlap matrix (TOM) and hierarchically clustered. These clusters are merged if not too dissimilar. After testing the modules for their significance (p-value threshold of 0.05, 10 bins and 100

permutations), the remaining modules are tested regarding the temporal variation (sample size is minimum of module size and 150, 1,000 tests, order of conditions blood < thrombus, p-value threshold of 0.05). The remaining modules are added to the Seurat object using the `AddModuleScore` function (ctrl set to 5) and are reported for further visualization and discussion. All samples were processed using 100 genes from each of the 10 principle components. All samples were processed with a soft power of 7, the monocytes with a soft power of 10.

In order to quantify the changes between blood and thrombus per cell type, the cell type was annotated in the Seurat data and differential genes between thrombus and blood were calculated using Seurat's `FindMarkers` function with a fold change cutoff of 0.1.

Correlation analysis is carried out using `ggplot2` with the `stat_smooth` function using the `lm` (linear regression) smoothing function.

The artificial thrombus data were processed with 10X Genomics CellRanger v6.1.1 like the original data with the corresponding gene expression GRCh38-2020-A reference. For the antibody capture library, human antibody hashtags 7, 8 and 9 were added, as well as CITE-seq antibodies for CD41 and CD16. The resulting raw feature-barcode-matrix was read into Seurat. Cells with less than 100 or more than 6000 expressed features were removed, as well as cells with less than 300 UMIs or more than 10% mitochondrial content. The data were multiplexed using the three human HTO, and identified doublets were removed. The CITE-seq antibodies were added into a separate assay and are normalized using the CLR method with parameter `margin=2`. The data was merged, normalized and 3000 highly variable features were identified using the "vst" method in the remaining 6927 cells (Artificial Thrombus $n=3573$, Real Thrombus $n=2563$, Blood $n=791$). Subsequently the resulting Seurat object was scaled (on these highly variable features) and 50 principal components were called on the 3000 highly variable genes. A UMAP embedding was calculated on 15 PCs and 100 nearest neighbors. Clusters were identified using the `FindClusters` function by Seurat with a resolution set to 0.3. Differential comparisons were conducted using Seurat's `FindMarkers` function with a fold-change cutoff of 0.25.

Chemokine interactome analysis

Chemokine ligand-chemokine receptor interactions were collected from two different resources⁷³ and <https://www.rnssystem.com/pathways/chemokine-superfamily-pathway-human-mouse-lig-recept-interactions> (year of access: 2021). Interactions are either classified as antagonist, agonist or undefined. In general, the steps described by Armingol et al.⁷⁴ are followed for determining cell-cell communications. The experimental expression data (for each cluster) is read in and filtered to only contain genes from the above collection of chemokine interactors. For each ligand-receptor pair, and for each cluster-pair, the communication score is calculated. This communication score is the product of the ligand expression and the receptor expression (expression product).

This results in a data frame in which for each ligand-receptor pair in each cluster pair a score is associated. To determine the total communication between two clusters, all communication scores between these clusters are summed.

In a second step, the data frame is arranged into matrix form, keeping only clusters of interest (or all, if no filtering was requested). The chord diagram (taken from https://github.com/tfardet/mpl_chord_diagram) displays the accumulated LR-interactions between clusters (all, or only for monocytes and neutrophils).

In addition, the matrix plot shows the scaled (z-score) expression scores for all interactions in the selected clusters. In a filtered version, only interactions which have at least in one cluster pair a z-score > 1 are shown. Finally, the chemokines overview displays the ligand-receptor map in the lower left corner, and shows the expression values for the receptors in the selected clusters on top, and those for the ligands to the right. This visualization allows for a concise overview of ligand and receptor expressions, together with an overview of possible LR-interactions. Source code for this analysis is available online https://github.com/mjoppich/chemokine_interactionmap.

scVelo

For the velocity analysis, the barcodes of all cells in the integrated Seurat object were written to disk per library. This list of barcodes is important for running `velocity`⁷⁵ if also barcodes are used that are not part of the filtered barcodes from CellRanger. Apart from specifying the barcodes of the required cells, `velocity` was run with default parameters. After performing the counting of unspliced RNAs using `velocity`, the acquired loom files were matched with the integrated Seurat object and the unspliced count matrix is written to disk together with a loomified version of the integrated Seurat object and additional meta information (e.g. UMAP coordinates). In the second step, this object is read using `scvelo`.⁴² The UMAP embedding is taken over and spliced (CellRanger counts) and unspliced (`velocity`) counts are stored in their respective layers. Genes that were not present in at least 50 cells were filtered out and the remaining matrix was normalized using `scvelo`'s `filter_and_normalize` function. 3000 highly variable genes were called using the Seurat-flavor before calculating PCs. In order to have a functioning neighbor graph, `bbknn` was called with `batch_key` identifying the single libraries (matching the integration strategy from Seurat) and neighbors within `batch=5`. The general `scvelo` vignette for performing velocity analyses was followed to calculate velocity in deterministic mode.

Monocle3 analysis

`Monocle3`¹⁷ was downloaded and installed on March 2023 from GitHub (cole-trapnell-lab/monocle3). The Seurat data objects were transformed into cell data set objects (RNA assay only), size factors were estimated and the data preprocessed using the `monocle3` functions `estimate_size_factors` and `preprocess_cds` with default parameters. From the Seurat object, gene names, clusters, UMAP embedding and PCA was transferred to the cell data set. Trajectories were learned using the `learn_graph` function with `use_partition=FALSE`, because the monocyte and neutrophil subsets already represent a single partition. Root cells for ordering cells by pseudo-time were selected such that these are most likely uninvolved in any hypothesis on phenotypic shifting and might represent

blood derived root cells (cluster 5 in the neutrophil and monocyte subsets). Finally, the pseudo-time distribution is visualized for each cluster in a bar plot.

Label transfer human and mouse neutrophils

For label transfer from human cluster labels to mouse cells, first human and mouse gene names were matched by upper-casing the mouse gene names. All data was subset to have only genes remaining which are present in both the human as well as the mouse dataset. The neutrophil subset was used as the human base object, and for mouse the neutrophils were subset from the global scRNA-seq object. The human and mouse scRNA-seq data were subsequently re-scaled. On the mouse subset, variable features were determined again and a new PCA was calculated with 50 principal components on each dataset. Subsequently, labels were transferred from the human neutrophil subset to the mouse subset. First, transfer anchors were identified with Seurat's FindTransferAnchor function using 10 transfer dimensions, at most 500 features and 20 anchor neighbors, 50 neighbors for filtering anchors and 15 cells to score anchors. The actual transfer was performed using Seurat's TransferData function using 10 neighbors for weighting anchors. The predicted cluster IDs from the human scRNA-seq were then presented on the mouse scRNA-seq dataset.

Neutrophil and PBMC isolation and pharmacological hypoxia mimicking

For further examination of neutrophil granulocytes we isolated granulocytes with the EasySep® Direct Human Neutrophil Isolation Kit (Stemcell Technologies, Cat# 19666), following the instructions provided by the manufacturer. PBMCs were isolated from whole blood with BD Vacutainer CPT tubes (BD Biosciences, Cat# 362780) and adjusted to a cell concentration of 10 million cells/ml.

The respective cells were distributed into 14ml Polystyrene Round-Bottom Tubes (Falcon, Cat# 352057). After centrifuging the tubes (350rcf, 4°C, 5 minutes) half of them was resuspended in a medium containing RPMI, 2mM L-Glutamin and 2% FBS, the other half in the same medium with additionally 50µM Roxadustat (Selleckchem, Cat# S1007) and incubated for 16 to 18 hours (37°C, 5% CO₂). Then, after another centrifugation and resuspension step, the samples were stained with the antibody mix and washed again.

Directly before flow-cytometry or FACS Sort, dead cell stain was added.

Non-classical and classical monocytes from the incubated PBMCs were FACS sorted with a BD FACSMelody™ Cell Sorter into RLT Plus Buffer with 1% β-mercaptoethanol and subsequently analysed by prime-seq.²⁰

Artificial coagulation activation and subsequent monocyte analysis

We used citrate coated tubes to take blood from healthy donors, which was afterwards filled into two Polystyrene Round-Bottom Tubes. After adding thrombin and calcium-chloride to one of the tubes and incubation for 4 hours, the coagulum was pushed through a 70 µm mesh, solved in PBS, centrifuged (350rcf, 7 minutes) and resuspended in flow-cytometry Buffer. Afterwards, the cell suspension from the coagulum and the blood from the other tube were incubated with the antibody master-mix. For the erythrocyte lysis, BD Pharm Lyse (BD Biosciences, Cat# 555899) was used. Directly before the Sorting process, dead cell stain was added.

FACS Sort was performed with the BD FACSMelody™ Cell Sorter, classical and non-classical monocytes were FACS-sorted.

In vitro fibrin clearance by CD16^{low} and CD16^{high} neutrophils

Human neutrophils were freshly isolated by EasySep Direct Human Neutrophil Isolation Kit (STEMCELL Technologies, #19666) and incubated with 50 µM Roxadustat for 24 hours as 1 million cells/ml in RPMI medium (RPMI medium (Bio&SELL GmbH, #BS.F1415) containing 10% FBS (Bio&SELL GmbH, #FBS.S.0615), and 2 mM glutamine (Gibco, #2146978)). Then the cells were pelleted by centrifugation at 320rcf, room temperature (RT) for 7 minutes. Cells were stained with APC anti-CD16 antibody (BioLegend, clone 3G8, #302012), and Hoechst 33342 (Invitrogen, #H3570)) for 20 minutes and then centrifuged at 320rcf, RT for 7 minutes. The supernatant was removed, and the cells were resuspended in RPMI containing 20% human plasma and 2 mM glutamine, normalized to 1 million cells/ml. ibiTreat µ-Slides VI 0.4 (Ibidi GmbH, #80606) used for in vitro clearance assays. Slides coating was performed with a mix of 155.6 µl of PBS, 6 µl of 8% human serum albumin (Sigma-Aldrich, #A9731-5G), 6 µl of human fibrinogen conjugated with AF488 (Invitrogen, #F13191), 2.4 µl of 100 mM CaCl₂, and 60 µl of human plasma. 10 µl of 100 U/ml thrombin was added to the coating mix just before transferring the mix into slides. The slides were then rested at room temperature for 15 minutes to allow attachment of the fibrin structures. Excessive clots were removed by flushing the slides with PBS using a 1 ml syringe. 1x10⁵ neutrophils from each sample were topped up to 150 µl using RPMI containing 20% human plasma and added to the slides. The slides were centrifuged at 40 rcf, RT for 7 minutes to let cells settle and then incubated at 37°C with 5% CO₂ for 16 hours. Imaging of the slides was performed immediately after incubation using an IX 83 Olympus Epifluorescence microscope. The cleared area of each cell was quantified using Fiji 2.10.0 software.

Flow cytometry of thrombus neutrophils and monocytes at different timepoints after artificial thrombus induction

Donor blood (n=4) was drawn into S-Monovette® Citrate 9NC blood collection tubes and artificial thrombi were generated through the addition of CaCl₂ and Thrombin to 3ml donor blood, as previously described, and rapidly mixing the sample with a transfer pipette in a 15ml falcon tube. Artificial thrombi were incubated at 37°C and 5% CO₂ for 5mins, 4hrs, 8hrs, 16hrs, 24hrs and 32hrs. At the end of each timepoint the thrombi were pressed through a 70µm filter and the resulting filtrate was depleted of red blood cells through two 13 minute incubations with BD Pharm Lyse™ lysing buffer (BD Cat. #555899) at RT. After a washing step (300g, 10 mins at 4°C), the sample was resuspended in human Fc-receptor blocking antibody which was incubated for 10mins at 4°C. Following this, conjugated antibodies against CD14 (FITC Biolegend #301803), CD45 (APC-Cy7 Biolegend #368515), CD16 (PE-Cy7

Biolegend #302015), CD15 (APC Biolegend #301907) were added and incubated for 20mins at 4°C. Following a final centrifugation step (300g, 10mins at 4°C), the sample was resuspended in flow-cytometry buffer. SYTOX™ Orange dead cell stain (0.1µM) (ThermoFisher Cat. #S34861) was added and the sample was immediately analysed on the BD FACSMelody™ cell sorter. Quantification of CD16 expression was performed with the FlowJo software (v10.8).

Flow cytometry of Roxadustat-stimulated neutrophils

Human neutrophils were freshly isolated by EasySep Direct Human Neutrophil Isolation Kit (STEMCELL Technologies, #19666). The cells were seeded as 1 million cells/ml in RPMI medium (RPMI medium (Bio&SELL GmbH, #BS.F1415) containing 10% FBS (Bio&SELL GmbH, #FBS.S.0615), and 2 mM glutamine (Gibco, #2146978)). Roxadustat (Selleckchem, #S1007) was added at final concentrations of 200 µM or 50 µM, respectively. The solvent DMSO was used as a control. Cells were subsequently incubated at 37°C with 5% CO₂ for 24 hours. Cells were subsequently collected by centrifugation at 320rcf, RT for 7 minutes. Cells were stained with FITC anti-CD45 antibody (Biolegend, 982316), PE/Cy7 anti-CD15 antibody (Biolegend, 323030), and APC anti-CD16 antibody (Biolegend, 302012) for 20 minutes at room temperature. After the staining, cells were centrifuged at 320rcf, RT for 7 minutes and then resuspended in 300 µl of FACS buffer (PBS with 0.5% BSA (Albumin Fraction V, Carl Roth GmbH & Co. KG, #8076.4) and 2 mM EDTA (AppliChem GmbH, #A4892)). Sytox Blue live/dead dye (Invitrogen, #S34857) was added at a final concentration of 1 µM before the flow cytometry experiment (LSRFortessa Flow Cytometer, BD Bioscience). Flow cytometry data were analyzed using FlowJo software (BD Bioscience, version: 10.8.14).

Flow Cytometry Sort, staining and microscopy of neutrophils and monocytes from artificial thrombi

Donor blood was drawn into S-Monovette® Citrate 9NC blood collection tubes and gently inverted. Artificial thrombi were generated as described previously. Artificial thrombi were incubated for 24hrs at 37°C and 5% CO₂. Following this, thrombi were processed as described previously. The resulting filtrate was erylysed with BD Pharm Lyse™ lysing buffer (BD Cat. #555899) twice for 10 minutes at RT, centrifuged (300g, 10mins at RT) and resuspended in human Fc-receptor blocking antibody which was incubated for 10mins at 4°C. Following this, conjugated antibodies against CD14 (FITC Biolegend #301803), CD45 (APC-Cy7 Biolegend #368515), CD16 (PE-Cy7 Biolegend #302015), CD15 (APC Biolegend #301907) were added and incubated for 20mins at 4°C. Following a final centrifugation step (300g, 10mins at 4°C), the sample was resuspended in PBS containing 0.5% BSA (FACS buffer). SYTOX™ Orange dead cell stain (0.1µM) (ThermoFisher Cat. #S34861) was added and the sample was immediately analysed and sorted on the BD FACSMelody™ cell sorter. Approximately 50,000 CD16^{high} and CD16^{low} monocytes/neutrophils were sorted into flow-cytometry tube containing 0.2ml flow-cytometry buffer. Following this, the sorted cells were centrifuged (300g, 10mins at 4°C), resuspended in flow-cytometry buffer and plated on Poly-L-lysine coated glass slides for 30 mins to allow attachment. Excess liquid was removed and diluted trypan blue was added after which a coverslip was added and the cells were imaged under brightfield with a Leica DM6B microscope. Sorted CD16^{high} and CD16^{low} neutrophils were additionally stained with MPO (R&D Systems Cat. #AF3667) and DAPI.

Immunofluorescence staining and quantification of thrombus neutrophils in mouse thrombi

The IVC was embedded in OCT, stored at -80°C and cut with a cryotome (CryoStar NX70 Kryostat, ThermoFisher Scientific). Samples were fixed with 4% formaldehyde and blocked with the respective serum (either goat serum, or donkey serum, containing 1% BSA and 0.5% Saponin). In *Nr4a1^{-/-}* and *Nr4a1^{+/+}* mouse thrombus sections neutrophils were visualized by anti-Ly6G (clone: 1A8; isotype: rat IgG2a) and MPO (either rabbit polyclonal, #GA51161-2, DAKO;; or goat anti human/mouse R&D Systems Cat. #AF3667). For PLAUR staining, rabbit anti human/mouse/rat PLAUR (Bioss #Bs-1927R) was used. Alexa labeled secondary antibodies (Invitrogen) were used for detection. DNA staining was performed using Hoechst (Invitrogen, Cat. # H3570). Finally mounting medium (DAKO) was applied to place a cover slip. The image acquisition was carried out by using a Zeiss Axio imager microscope with an AxioCam. After image acquisition, cells were manually counted. For quantification of NETS three criteria had to be fulfilled: (1) Presence of extracellular DNA protrusions, (2) the protrusion has to originate from a Ly6G-marked cell, (3) the DNA-structure has to be decorated by MPO.

To visualize neutrophils and urokinase expression in human thrombus, we used Hoechst dye (Invitrogen, Cat. # H3570), anti-MPO (R&D systems, Cat. # AF3667), and anti-Urokinase (Abcam, Cat. # ab24121). The imaging was performed by the ZEISS LSM880 (Confocal, Serial # 3851003082) Axio Imager.M2 (Carl Zeiss Microscopy GmbH, Göttingen) or Leica DM6B microscope and analysis was performed on the QuPath platform (v0.50) or using FIJI (ImageJ) or AxioVision (Zeiss).

Immunohistochemical analyses in human FFPE or fresh frozen thrombi

FFPE and fresh frozen thrombi were analyzed in an anonymized manner. For uPA staining in fresh frozen tissue, samples were fixed with 4% formaldehyde and blocked with goat serum (containing 1% BSA and 0.5% Saponin). Subsequently (Abcam, Cat- #ab24121) Rabbit anti-uPa, and goat anti MPO (R&D Systems, Cat. #AF3667) were added to the samples. After a washing step, Alexa labeled secondary antibodies (Invitrogen) were used for detection. DNA staining was performed using Hoechst (Invitrogen, Cat. #H3570). After a final washing step, fluorescent mounting medium (DAKO, Cat. #S3023) was applied to place a cover slip. For FFPE thrombi, tissue was deparaffinized (using different concentrations of Xylo and Ethanol), antigen retrieval was performed by boiling in Tris-EDTA Buffer (containing: 2.5 mL 1M Tris base, 0.5 ml 0.5M EDTA, 0.125 mL Tween-20, water 247ml, adjusted to pH 9.0). After a subsequent blocking step with 10% Donkey serum and 0.3% Triton X-100 the following primary antibodies were added: Goat Anti MPO (AF3667 R&D Systems), Rabbit Urokinase (AB24121 Abcam). After a washing step Donkey anti-goat AF647 and Donkey anti-rabbit

AF488 were added and Hoechst was added before the final washing step. Slides were mounted in DAKO Fluorescent Mounting Medium #S302380. Immunofluorescence images were made using ZEISS LSM880 (Confocal, Serial # 3851003082) Axio Imager.M2 (Carl Zeiss Microscopy GmbH, Göttingen) or Leica DM6B microscope and analysis was performed using FIJI (ImageJ) or AxioVision (Zeiss).

Automated immunohistochemistry for analysing frequencies of immune cell subsets was performed using automated BenchMark ULTRA IHC-System, Roche Diagnostics, Rotkreuz, Switzerland. Antigen retrieval was performed using CC1 Antigen Retrieval buffer, Roche Diagnostics, Rotkreuz, Switzerland according to the manufacturer's protocol. Antibodies as used are listed below. Stainings were visualized using ultraView Universal DAB Detection Kit and counterstained with hematoxylin and bluing solution, all supplied by Roche Diagnostics, Rotkreuz, Switzerland. Whole slides were scanned using Aperio GT 450 DX Slide Scanner, Leica Biosystems, Wetzlar, Germany. Digital Slides were analyzed using the positive cell detection tool within the open-source software QuPath. Automated positive cell detection results were visually checked for plausibility by an experienced pathologist.

Target	Manufacturer	Host Species	Clonality	Clone	Dilution	Reagent	Temperature	Time
						Antigen retrieval		
CD3	Zytomed Systems GmbH, Berlin, Germany	Rabbit	monoclonal	SP7	1:150	CC1	37°C	64 min
CD4	Leica Biosystems, Wetzlar, Germany	Mouse	monoclonal	4B12	1:500	CC1	37°C	64 min
CD8	Cell Marque Tissue Diagnostics, Rocklin, California, US	Mouse	monoclonal	C8/144B	1:50	CC1	37°C	64 min
CD14	Zytomed Systems GmbH, Berlin, Germany	Rabbit	monoclonal	EPR3653	1:150	CC1	37°C	36 min
CD15	Abcam, Cambridge, UK	Mouse	monoclonal	LEU-M1	1:500	CC1	37°C	36 min
CD20	DAKO GmbH, Jena, Germany	Mouse	monoclonal	L26	1:400	CC1	37°C	36 min

Neutrophil infiltration and thrombus regression upon Reparixin or control treatment in artificial thrombi

Donor blood (n=5) was drawn into S-Monovette® Citrate 9NC and EDTA K3E blood collection tubes, for subsequent artificial thrombus generation and neutrophil isolation respectively. Artificial thrombi were induced as described previously, the samples were then incubated at 37°C and 5% CO₂ for 3 hours. Neutrophil isolation from donor blood was performed using the EasySep™ Direct Human Neutrophil Isolation Kit (StemCell Cat. #19666) according to the manufacturer's instructions. Isolated neutrophils were then labelled with CellTracker™ Red CMTPX Dye (ThermoFisher Cat. #C34552) and resuspended at the concentration of 1 million cells/ml of donor-matched plasma which was treated with 20µM Reparixin (Selleckchem Cat. #S8640) or the vehicle control. Artificial thrombi were weighed, prior to the addition of labelled neutrophils, and subsequent weight recordings was taken at 12 hours after which thrombi remnants were fixed in 4% PFA for 30mins and placed in 30% sucrose at 4°C overnight. Fixed thrombi were then embedded in O.C.T. compound, frozen at -80°C and then cut into 10µm sections which were fixed with 4% PFA and stained with DAPI (Merck Cat. # 10236276001). Images were acquired with a Leica DM6B microscope imaging 5 fields of view (FOV) per section and 3 sections per thrombi. Image analysis was performed on the QuPath platform (v0.50) where the proportion of labelled neutrophils to total cells per field-of-view was calculated.

ROTEM Analysis

We used rotational thromboelastometry (ROTEG-05, Pentapharm GmbH, Munich, Germany) to measure the different coagulative capacities of murine whole blood from wildtype and Nur77^{-/-} mice under low shear stress conditions, comparable to those in the lower Vena cava. Murine blood was drawn into citrate tubes (#04.1952.100, SARSTEDT AG & Co. KG, Nuembrecht, Germany) immediately analyzed. Therefore, we mixed 300 µl of murine whole citrate blood with 20 µl StarTEG solution (#503-10, Tem Innovations GmbH, Munich, Germany) and 20 µl EXTEM solution (#503-05, Tem Innovations GmbH, Munich, Germany) in reagent cups (#200011, Tem Innovations GmbH, Munich, Germany) and measured clotting time (CT), clot formation time (CFT), maximum clot firmness (MCF) and maximum lysis (ML) at 37 °C.⁷⁶

Antibody*

*Not every single antibody used for staining was shown or used for analysis.

Flow-cytometry Phenotyping

Color	Antigen	Company	Cat. #
BV650	CD45	BioLegend	304044
FITC	CD14	BD Pharmingen	557153
PERCP-Cy5.5	Siglec 8	BioLegend	347107
APC	CD15	BioLegend	301908

(Continued on next page)

Continued

Color	Antigen	Company	Cat. #
APC-Cy7	CD19	BioLegend	363010
BV605	HLA-DR	BioLegend	307640
BV785	CD123	BioLegend	306032
BV510	CD3	BioLegend	317332
BV711	CD56	BioLegend	362542
AF700	CD34	BioLegend	343622
Pacific Blue	CD41	BioLegend	303714
SytoxOrange	Nucleic acid stain	Invitrogen	S11368

Flow-cytometry Neutrophil^a

Color	Antigen	Company	Cat. #
BV650	CD63	BioLegend	353026
FITC	CD177	BioLegend	315804
PE	VEGFR-1	MACS Miltenyi Biotec	130-124-438
PERCP-Cy5.5	TCR α/β	BioLegend	306724
APC	CD15	BioLegend	301908
APC-Cy7	CD184	BioLegend	306528
BV605	CD49d	BioLegend	304324
BV785	CD62L	BioLegend	304830
BV510	CD16	BioLegend	302048
BV711	CD11b	BioLegend	301344
AF700	IL-17A	BioLegend	512318
PE-Dazzle	CD31	BioLegend	303130
PE-Cy7	CD284	Invitrogen	25-9917-42
SytoxBlue	Dead cell stain	Invitrogen	S34857

^a In the Roxadustat *in vitro* experiment group, CD87 in PE (Biolegend, Cat.: 336906) and CD177 in PE-Dazzle (Biolegend, Cat.: 313226) were used for analysis.

Flow-cytometry Monocyte

Color	Antigen	Company	Cat. #
BV650	CD45	BioLegend	304044
FITC	CD14	BD Pharmingen	557153
PE	CD93	BioLegend	336108
PERCP-Cy5.5	CD36	BioLegend	336224
APC	SLAN	MACS Miltenyi Biotec	130-117-919
APC/Fire 750	IgE	BioLegend	325516
BV605	HLA-DR	BioLegend	307640
BV786	CD192	BioLegend	357234
BV510	CD16	BioLegend	302048
BV711	CD86	BioLegend	305440
AF700	CD11c	BioLegend	337220
PE-Dazzle	CD11a	BioLegend	301232
PE-Cy7	CD9	BioLegend	312116
SytoxBlue	Dead cell stain	Invitrogen	S34857

Flow-cytometry Sort Panel for Neutrophils and Monocytes

Color	Antigen	Company	Cat. #
FITC	CD45	BioLegend	368508
PB	CD14	BD Biosciences	558121
PE-Cy7	CD16	BD Biosciences	557744
PERCP-Cy5.5	Siglec 8	BioLegend	347107
APC	CD15	BioLegend	301908
APC-Cy7	CD19	BioLegend	363010
BV510	CD3	BioLegend	317332
AF700	CD34	BioLegend	343622
SytoxOrange	Dead cell stain	Invitrogen	S11368

Flow-cytometry Sort Panel for non-classical and classical Monocytes

Color	Antigen	Company	Cat. #
FITC	CD14	BD Pharmingen	557153
PE-Cy7	CD16	BD Biosciences	557744
APC-Cy7	CD56	BioLegend	362512
PE	CD3	BioLegend	An
PE	CD20	BioLegend	302306
SytoxRed	Dead cell stain	Invitrogen	S34859

QUANTIFICATION AND STATISTICAL ANALYSIS

Quantification and statistical analysis

If not specified otherwise, values were tested for normal distribution and t-test (two-tailed if not specified otherwise) or Mann-Whitney test were performed to compare groups as indicated, if not specified otherwise. Paired data were tested by paired t-test (if normally distributed) or Wilcoxon matched-pairs signed rank test (if not). If no further p-value is depicted in graphs tested for statistical significance, then no significant difference was detected. A value of $P < 0.05$ was considered significant.